Functionalized multi-walled carbon nanotubes supported Ni-based catalysts for adiponitrile selective hydrogenation to 6-aminohexanenitrile and 1,6-hexanediamine: Switching selectivity with [Bmim]OH

Yang Lv [a], Haishuai Cui [a], Pingle Liu [a,b,c,*], Fang Hao [a], Wei Xiong [a,*], He'an Luo [a,b,c]

[a] College of Chemical Engineering, Xiangtan University, Xiangtan 411105, China
[b] National & Local United Engineering Research Centre for Chemical Process Simulation and Intensification, Xiangtan University, China
[c] Engineering Research Centre for Chemical Process Simulation and Optimization, Ministry of Education, Xiangtan University, China

ARTICLE INFO

ABSTRACT

Functionalized multi-walled carbon nanotubes supported nickel-based catalysts were prepared and applied in adiponitrile (ADN) hydrogenation. The characterization results show that different functional groups such as NH_2-, $COOH-$, $OH-$ on MWCNTs surface can effectively act on metal ions by electrostatic attractions and chemical interactions so as to provide nucleation sites, and N species in MWCNTs can act as active sites for Ni deposition due to the strong electronic interactions between N species and Ni so as to promote ultra-small Ni nanoparticles formation, decrease NiO reduction activation energy, increase zero-valent Ni amounts as well as Ni nanoparticles dispersion. Furthermore, the doped N increases the lewis basicity, which favors the formation of primary amine of 6-aminohexanenitrile (ACN) and 1,6-hexanediamine (HDA). Moreover, the basic ionic liquid [Bmim]OH may switch the selectivity by inhibiting nucleophilic addition of the primary amine to the α-carbon of aldimine *via* the stabilization of $-NH_2$ groups in the amino-imine intermediates so as to impede by-products formation. In addition, the mechanism for ADN hydrogenation in [Bmim]OH was studied by density functional theory calculations. Under optimized conditions, it gives 97.80% total selectivity to ACN and HDA at 95.34% ADN conversion over Ni/N-MWCNTs-800 in the presence of [Bmim]OH.

© 2019 Elsevier Inc. All rights reserved.

1. Introduction

Hydrogenation of nitrile compounds to corresponding primary amines is one of actively investigated research topics in the bulk and fine chemical industries [1]. Primary amines are important chemical raw materials and fine chemical intermediates, which can be widely used in synthetic plastics, detergents, textile additives, flotation agents, antistatic agents and preservatives, etc. [1]. Nevertheless, in the process of nitriles hydrogenation to primary amines, hydrogenation and condensation can take place simultaneously in the unsaturated $-C\equiv N$ bond. Hence, the formation of primary amines is often accompanied by secondary, tertiary amine and other by-products [1]. Thus, the key step to improve the selectivity to primary amines is to inhibit the formation of the above mentioned by-products.

ADN hydrogenation to ACN and HDA is a typical route of nitriles hydrogenation. ACN is an important intermediate to produce ε-caprolactam (CPL), the monomer for the production of Nylon-6 and fibers, and HDA is the raw material for producing Nylon-66 [2]. It can be seen from Path 1 that ADN hydrogenation is a complex process with different reaction pathways. Firstly, semi-hydrogenation of ADN produce highly active imines, which can be hydrogenated to primary amines of ACN and HDA, and intermediate imines can also react with primary amines through nucleophilic addition of the primary amine to the α-carbon of aldimine to form 1-(alkylamino)alkane-1-amine (intermolecular condensation) and azacycloheptane-2-amine (intramolecular condensation), then it can be further deaminated to form N-substituted imines (tertiary amine), followed by hydrogenation to main by-products of secondary amines 1-azacycloheptane (ACH) [3–5].

At present, Raney-type catalyst [6,7], Ziegler-type catalyst [2], amorphous alloy catalyst [8–10], non-supported [3–5,11,12] and supported Ni-based catalysts [13–22], precious-metal catalyst
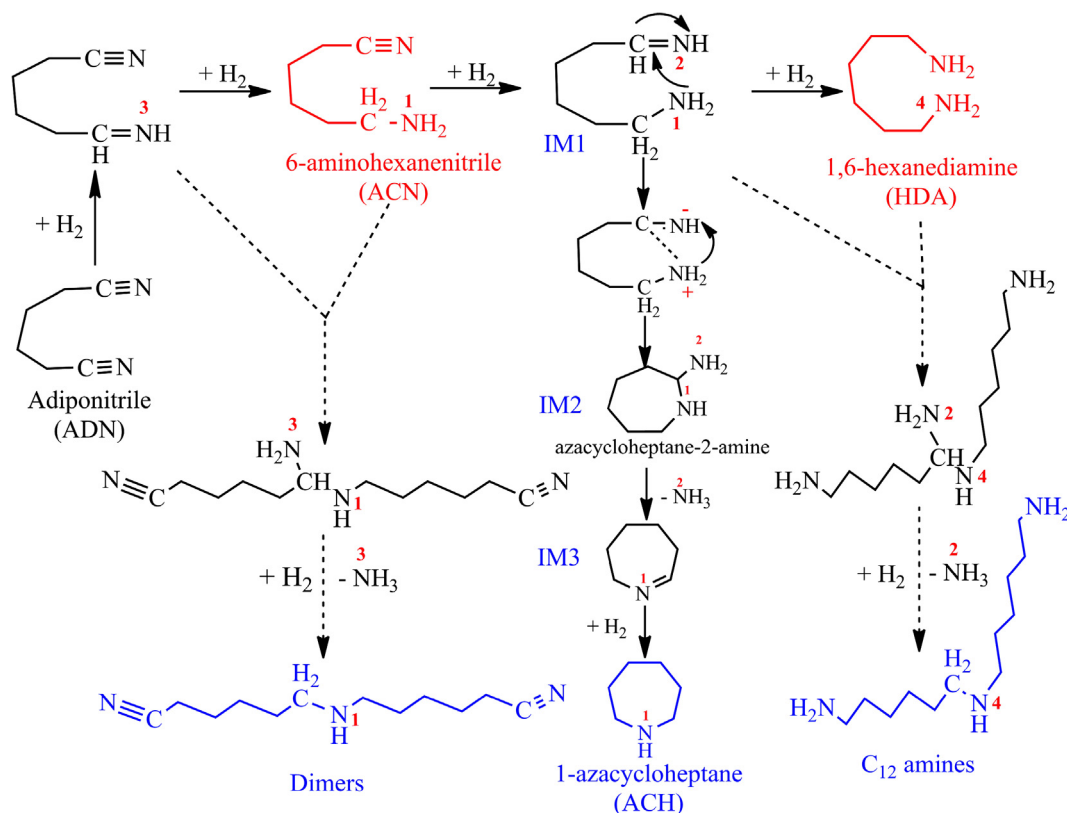
Path 1. Formal reaction scheme for adiponitrile hydrogenation.

such as Ru or Rh have been reported for ADN hydrogenation [23,24]. ADN hydrogenation over Raney-type catalyst has the problems of fragmentation, spontaneous combustion and requirement of a large amount of ammonia and alkali solutions to suppress the side reactions [6,7,9,10]. ADN hydrogenation catalyzed by Ni-P amorphous catalyst under atmospheric pressure showed that the special structure of amorphous alloy lead to high selectivity to HDA due to that the addition of P changed the properties of Ni active sites [9,10]. Gas phase hydrogenation of ADN over MgO/Ni catalyst obtained from NiO octahedral crystal precursor gave 87% selectivity to ACN at 83% ADN conversion under very high space velocity and high H_2/ADN ratio [3,4]. Fe_2O_3, α-Al_2O_3, γ-Al_2O_3 and graphite supported Ni-based catalysts and non-supported K_2O/Ni catalysts were prepared by F. Medina and applied in gas phase ADN hydrogenation [11–15], and it was found that the doped K provides more surface basic sites, which favors the formation of primary amine of ACN and HDA [11,12,14,16–18,20,21]. Moreover, Ru complex homogeneous catalyst and Rh supported catalyst showed high conversion and selectivity in ADN to ACN and HDA in liquid phase hydrogenation, however, these catalysts possess some disadvantages such as complex preparation process, high cost and requirement of large amount of ammonia and alkali solutions to inhibit the formation of by-products [23,24]. Additionally, layered double hydroxide Ni/Mg/Al catalysts were prepared by coprecipitation and used in liquid phase ADN hydrogenation, and it gave 66% selectivity to ACN at 70% ADN conversion with 0.60/0.15/0.25 optimal molar ratio of Ni/Mg/Al under 353 K and 2.5 MPa H_2 pressure [5]. Recent work by our group revealed that the synergistic effect between the active Ni metal and promoter such as K, Fe, La and Cu can significantly enhance the catalytic activity, and the selectivity to primary amine of ACN and HDA was effectively promoted over K and MgO doped catalysts [16–18,20–22].

Multi-walled carbon nanotubes (MWCNTs) can be widely used as supports due to high electrical conductivity, high adsorption capacity, large surface area, low mass-transfer resistance, and controllable surface properties, which can provide nucleation centers as well as adjust the surface electronic chemical environment of metal nanoparticles [25,26]. Functional species and heteroatom doped MWCNTs can effectively increase the metal nanoparticles dispersion, suppress sintering resistance, and regulate chemical state of active components, and thus can influence the catalytic performance [25–33]. Chen et al. reported that the interaction between cobalt nanoparticles and oxygen- and nitrogen functionalized carbon nanotubes will obviously boost catalytic hydrogenation of nitrobenzene due to ultra-dispersed cobalt nanoparticles and higher cobalt reducibility [31]. Moreover, Shi et al. also found that ultrasmall-sized Pt nanoparticles (∼1 nm) formed in nitrogen and oxygen functional groups modified MWCNTs due to the energetic interaction between metal nanoparticles and support, and these catalysts showed superior catalytic performances in nitroarenes hydrogenation [33].

Basic ionic liquids (B-ILs) have attracted significant research interest, it can be used as environmental-friendly solvents since they are flexible, non-volatile, non-corrosive, insoluble in a variety of organic solvents, thus overcome the disadvantages such as a large amount of waste production, severely corrosive environment, difficulty in catalyst recovery and prone to saponification caused by using of traditional inorganic bases such as NaOH, KOH or some commonly amine organic solvents, and it can also be used as superior reaction mediators since it can effectively enhance the selectively *via* stabilization of reactive intermediates and it is easy to be recovered in catalytic process [34–37]. Moreover, B-ILs can provide a new trend for the development of environment-friendly basic catalysts that combine the advantages of the inorganic bases and ILs.

In this work, Ni nanoparticles supported on NH_2—, COOH—, OH— and N species modified MWCNTs were prepared and applied in ADN hydrogenation to ACN and HDA under very mild conditions, and the synergistic effect between Ni nanoparticles and functional groups or doping N species on the surface of MWCNTs were explored. Furthermore, small amount of basic ionic liquids 1-butyl-3-methylimidazolium hydroxide ([Bmim]OH) were used as a switch for adjusting the selectivity to primary amines of ACN and HDA, it was found that it is of great effective strategy to achieve high selectivity to ACN and HDA. Additionally, density functional theory (DFT) calculations were applied to explore the insight of ADN hydrogenation in the presence of [Bmim]OH.

2. Experimental

2.1. Materials

The 99 wt% adiponitrile, 98.5 wt% 1,6-hexanediamine and 98 wt% 6-aminocapronitrile were supplied by J&K scientific LTD. The 98 wt% $Ni(NO_3)_2 \cdot 6H_2O$, 99 wt% $FeSO_4 \cdot 7H_2O$, 99.9 wt% $(NH_4)_2CO_3$, 98.5% wt.% KSCN, 97% wt.% NaOH, 99% wt.% melamine, 99.0% wt.% tetrahydrofuran (THF), 99% wt.% dichloro sulfoxide ($SOCl_2$), 99.5% wt.% ethylic acid, formaldehyde solution, NaClO solution were purchased from Shanghai Macklin Biochemical Co., Ltd. The 98% wt.% H_2SO_4, 68% wt.% HNO_3, 38% wt.% HCl and 28% wt.% $NH_3 \cdot H_2O$ were bought from Sinopharm Chemical Reagent Corporation Limited. The 99.7 wt% ethanol was provided by Fuyu Fine Chemical Co. LTD. The basic ionic liquids ([Bmim]OH) was supplied by Shanghai Cheng Jie Chemical Co. LTD. Multiwalled carbon nanotubes (MWCNTs) were purchased from Shenzhen Nanotech Port Co. LTD. The 99.99% H_2 and 99.99% N_2 were bought from Zhuzhou Diamond Gas Company.

2.2. Synthesis of the support

2.2.1. Synthesis of COOH-MWCNTs

Typically, 2 g pristine MWCNTs were dispersed into 100 mL solution of concentrated HNO_3/H_2SO_4 (volume ratio is 1:3) and treated under ultrasonic oscillation for 1 h. Subsequently, the suspension was treated under refluxing and stirring at 373 K in oil bath for 12 h, followed by washing with distilled water repeatedly until pH is neutral and separated by centrifugalization, and then dried in vacuum at 323 K to obtain COOH-MWCNTs.

2.2.2. Synthesis of NH2-MWCNTs

Firstly, 2 g COOH-MWCNTs were placed in a three-necked bottle, 40 mL dichloro sulfoxide ($SOCl_2$) was added and refluxed at 343 K for 24 h. The solid was separated and washed repeatedly with tetrahydrofuran (THF) and then dried in vacuum. Secondly, the treated MWCNTs and 5 g $(NH_4)_2CO_3$ were placed in a three-necked bottle, followed by adding 100 mL concentrated ammonia water and stirring for 6 h, and then filtered, washed with distilled water repeatedly and dried in vacuum. Thirdly, 30 mL sodium hypochlorite was added in the treated MWCNTs in ice bath for 2 h, then moved to 343 K water bath for 2 h, and then cooled, filtered, washed repeatedly with distilled water and dried in vacuum at 323 K to obtain NH_2-MWCNTs.

2.2.3. Synthesis of OH-MWCNTs

Firstly, 2 g pristine MWCNTs were added in 100 mL 5 mol/L hydrochloric acid solution, and then refluxed and stirred for 12 h at 353 K. Secondly, the treated MWCNTs were added in the solution of $FeSO_4 \cdot 7H_2O$ with pH value of 3, followed by stirring under ultrasonic for 1 h at 303 K. Thirdly, the suspension was quickly dripped into 75 mL H_2O_2 in 5 min through a droplet funnel, and then stirred under ultrasonic for 24 h. Finally, the mixture was

washed by 2 mol/L HCl and distilled water repeatedly until the pH = 7 and no Fe^{3+} exist (detected by KSCN solution), followed by separating and drying in vacuum at 323 K to obtain OH-MWCNTs.

2.2.4. Synthesis of N-MWCNTs-T

Typically, 2 g pristine MWCNTs were dispersed into 100 mL concentrated nitric acid (68 wt%) solution for 24 h at 348 K, then dried in vacuum at 323 K for 12 h. Subsequently, 1 g treated MWCNTs and 1 g melamine were added to the flask, and then a certain amount of water and formaldehyde were added and stirred under ultrasonic for 2 h at 303 K, followed by adding small amount of 1 mol/L sodium hydroxide solution to adjust the pH value to 10, and then stirred under ultrasonic for 1 h at 348 K. Afterward, the suspension was cooled to 303 K and small amount of ethylic acid was added to adjust the pH value to 5, and then stirred for 24 h and dried at 353 K for 12 h. Finally, the mixture was heated and roasted in a tube furnace under the protection of N_2 (the heating rate is 2 K/min) for 2 h under different pyrolysis temperature to obtain the N-MWCNTs-T (T represents pyrolysis temperature).

2.3. Catalyst preparation

The functionalized MWCNTs (F-MWCNTs) supported Ni catalysts were prepared by wetness impregnation-reduction method. Firstly, a certain amount of deionized water and 0.5 g F-MWCNTs were added to the flask, then stirred under ultrasonic at 303 K for 1 h. Secondly, a certain amount of metal precursor $Ni(NO_3)_2 \cdot 6H_2O$ was dissolved in deionized water and dropped into the suspension of F-MWCNTs, then stirred under ultrasonic for 2 h at 303 K. Thirdly, the suspension was evaporated until the ratio of liquid-to-solid is 5 mL·g^{-1}, then impregnated under violent stirring for 10 h at 303 K. Finally, the suspension was dried in vacuum at 383 K for 12 h to obtain the catalyst precursors. After that, the catalyst precursors were putted into a tube furnace and calcined at 623 K for 4 h under 50 mL/min N_2, followed by switching the N_2 to 50 mL/min H_2 for another 4 h to obtain F-MWCNTs supported Ni catalysts.

2.4. Catalyst characterization

N_2 physisorption isotherms were performed by using Micromeritics ASAP 2020. Typically, all the samples were degassed for 16 h in vacuum at 473 K before the test and measured at 77 K by using nitrogen as adsorbent.

X-ray diffraction (XRD) was recorded on D/max 2500 TC diffractometer, Cu Kα radiation (18 kW, 60 kV, 300 mA) was used as the diffraction source, and it was scanned over the 2 θ range of 5–90° in the steps of 0.02°.

The SHIMADZU-Kratos Kratos Axis Ultra[DLD] spectrometer was used to record XPS patterns. Typically, the emissive source was Al Kα (1486.6 eV) and the range of scanning energy was 0–1200 eV with 1 eV steps. Moreover, the binding energies of all the samples were corrected by contaminate C (C 1s = 284.6 eV).

Fourier transform Infrared spectra (FT-IR) were carried out on Nicolet-Nexus 670 spectrometer with KBr pallets. And the scanning range was from 400 cm^{-1} to 4000 cm^{-1} with the 0.6329 cm$^{-1} \cdot$s^{-1} scanning rate and 1.0 cm^{-1} intervals.

Raman spectra were performed on Renishaw 21,000 Raman spectrometer, and it was equipped with 545.5 nm laser source with 200–4000 cm^{-1} scanning range.

TEM characterizations were carried out on a JEOL 2010 FEG microscope equipped with HAADF-STEM detector. The acceleration voltage was 200 kV, the point resolution was 0.23 nm and the maximum magnification range was 2000–1500000. The method of sample preprocessing was as follow: the sample was suspended in anhydrous ethanol after fine grinding, and then treated with ultrasonic for 30 min, followed by extracting and dripping the

supernatant on the copper net coated with carbon film and dried at 323 K for 10 min before test.

Scanning electron microscope (SEM) was conducted on HITACHI S4800 with the 1–30 kV range of acceleration voltage. The electron emission source was the cold field emission source with semi-submerged objective lens. And the resolution of secondary electronic graphics at low acceleration voltage was 2 nm as well as at high acceleration voltage was 1 nm. The sample needs to be dispersed in ethanol and dried on the copper mesh before testing.

Temperature programmed reduction (TPR) was conducted by using Quantachrome ChemBET-3000. 0.01 g sample was placed into U-shape quartz tube, and then increased the temperature to 573 K ($10 K·min^{-1}$) in the protection He flowing ($30 mL·min^{-1}$) and maintained at 573 K for half an hour, followed by cooling to 373 K under He flowing. Afterwards, switched the He to 10% H_2/Ar flowing ($30 mL·min^{-1}$), and then raised the temperature from 373 K to 1073 K ($10 K·min^{-1}$). The exhaust gas was dehydrated and dried by 5A molecular sieve, then entered into TCD detector and recorded the reduction state of the sample.

Ammonia temperature programmed desorption (NH_3-TPD) was performed on Quantachrome ChemBET-3000. The sample was placed in U-shape quartz tube and the temperature was increased the temperature to 673 K ($10 K·min^{-1}$) under He flowing ($30 mL·min^{-1}$) and maintained for 1 h, following by decreasing the temperature to 353 K. Subsequently, changed the He flowing to 10% NH_3-90% He with steady flowing rate of 30 mL·min^{-1} until the baseline becomes stable. Finally, replaced the 10% NH_3-90% He by He flowing and flushed for half an hour, and then raised the temperature to 1073 K ($10 K·min^{-1}$) in He flowing.

Carbon dioxide temperature programmed desorption (CO_2-TPD) was also measured on Quantachrome ChemBET-3000 and possessed a similar operating process as that of NH_3-TPD, except that the He flowing was substituted by 10% CO_2-90% He.

H_2 chemisorption was conducted on Quantachrome ChemBET-3000. The sample was firstly pre-treated at 623 K under 10% H_2-90% Ar ($30 mL·min^{-1}$) for 4 h in U-shape quartz tube, and then replaced the 10% H_2-90% Ar by 99.99% Ar ($30 mL·min^{-1}$) to sweep the adsorbed H_2 until the baseline becomes stable. Afterwards, the temperature was cooled to 303 K and the absorbed H_2 was analyzed by H_2 pulse titration method that 0.2 μL H_2 was injected repeatedly until the peak area remained unchanged. According to the stoichiometry of the surface metal atom adsorbed hydrogen molecule, the number of surface metal atom was obtained, and the metallic surface areas and metallic dispersion can be acquired (the cross-sectional area of Ni is $6.49 \times 10^{-20} m^2$).

2.5. Procedure for the catalytic test

The catalytic performance was carried out in a 100 mL stainless steel reactor equipped with temperature, pressure and speed controller. Firstly, 0.21 g catalyst, 15 mL 99.7 wt% ethanol and 1 g ADN were added to the PTFE inner lining in the reactor, then the reactor was sealed and the airtightness was checked *via* introducing 3 MPa N_2. Subsequently, the air in the reactor was replaced by N_2, then the reactor was vacuumized, and then a certain amount of H_2 was pumped in and it started to stir when the temperature and H_2 pressure was raised to the required value. Finally, the product was separated by centrifugation and analyzed by Agilent 7820A gas chromatography with DB-1701 (30 m × 0.32 mm × 0.25 μm) chromatographic column and using dimethyl phthalate as internal standard.

2.6. Theoretical calculations

First-principle calculations were carried out by using the DMOl3 in Material studio programs, which is based on the DFT Semi-core Pseudopots (DSPP) method. The k-point sampling was generated with a $1 \times 1 \times 1$ mesh. The self-consisdirect field (SCF) procedure with a convergence threshold of 10-5 au on the energy and electron density was used. The computational study of the reaction mechanism was performed on the GGA/PBE level. The transition state (TS) search was used by the complete LST/QST method until the transition state structure was determined.

3. Results and discussion

3.1. Characterization of the samples

3.1.1. N_2 physisorption isotherms

N_2 physisorption isotherms of the samples and their BJH pore size distribution are depicted in Fig. 1. The obvious type IV Langmuir isotherms with typical H2 type hysteresis loop at high relative pressure (>0.8 P/Po) in Fig. 1(a) and (b), together with the BJH pore size distribution of samples in Fig. 1(a1, b1), indicate that all the samples possess mesoporous structure. It can be observed that the physisorption isotherms of each sample are almost similar, which suggest that the morphology of the sample is preserved after the modification. Moreover, it can be seen in Fig. 1(b), the intensity of mesopores (3–5 nm) peak in Ni-based catalyst is weaker than the corresponding support, the reason may be that the mesopores are partially blocked by the Ni nanoparticles [38]. And the BET surface area, average pore diameter and pore volume of the samples are summarized in Table 1.

3.1.2. XRD

XRD patterns of functionalized MWCNTs and their corresponding Ni-based catalysts are illustrated in Fig. 2. As shown in Fig. 2-2, the diffraction peaks around 26.2°, 42.5° and 44.5° in MWCNTs and all the functionalized MWCNTs are corresponded to graphitic-type lattice (0 0 2), (1 0 0) and (1 0 1) planes respectively (JCPDS 75-1621) [22,38,39]. And the diffraction peaks at 44.5°, 51.8° and 76.3° in Fig. 2-1 are ascribed to metallic Ni (1 1 1), (2 0 0) and (2 2 0) planes (JCPDS 47-1049) [22,38,39]. It is notable that the characteristic peaks of all the N functionalized MWCNTs in Fig. 2 are slightly shifted toward lower 2θ values in comparison with other samples. The reason may that the doped N species enter the carbon lattice and distort its structure so as to form more defects and vacancies [40,41]. Moreover, it can be seen that the pristine MWCNTs (Fig. 2-2-f) possess the strongest intensity of (0 0 2) plane characteristic peaks and N-MWCNTs-800 (Fig. 2-2-c) exhibit the broadest full width at half maximum (FWHM) values in Fig. 2, it indicates that the pristine MWCNTs have more orderly structure and fewer defects than the functionalized MWCNTs, and N species functionalized MWCNTs under 1073 K pyrolysis temperature can result in more defects in the graphitic layers [41]. In addition, it can be observed from Fig. 2-1 that functionalized MWCNTs supported Ni-based catalysts display broader FWHM than Ni/MWCNTs (Fig. 2-1-f), especially Ni/N-MWCNTs-800 in Fig. 2-1-c, the weakest intensity of Ni (1 1 1) characteristic peaks implies ultra-small Ni crystallite size and homogeneously dispersed Ni nanoparticles. This phenomenon could be attributed that the functional group such as NH₂—, COOH—, OH— and N species can effectively act on Ni nanoparticles and provide nucleation sites so as to favor Ni nanoparticles dispersion, especially for N species, which have the strong stabilization effect and lead to form large numbers of defects.

3.1.3. Raman spectra

The surface electrons states and structural variation of functionalized MWCNTs and supported catalysts were characterized by Raman spectroscopy. As shown in Fig. 3, the typical peaks around
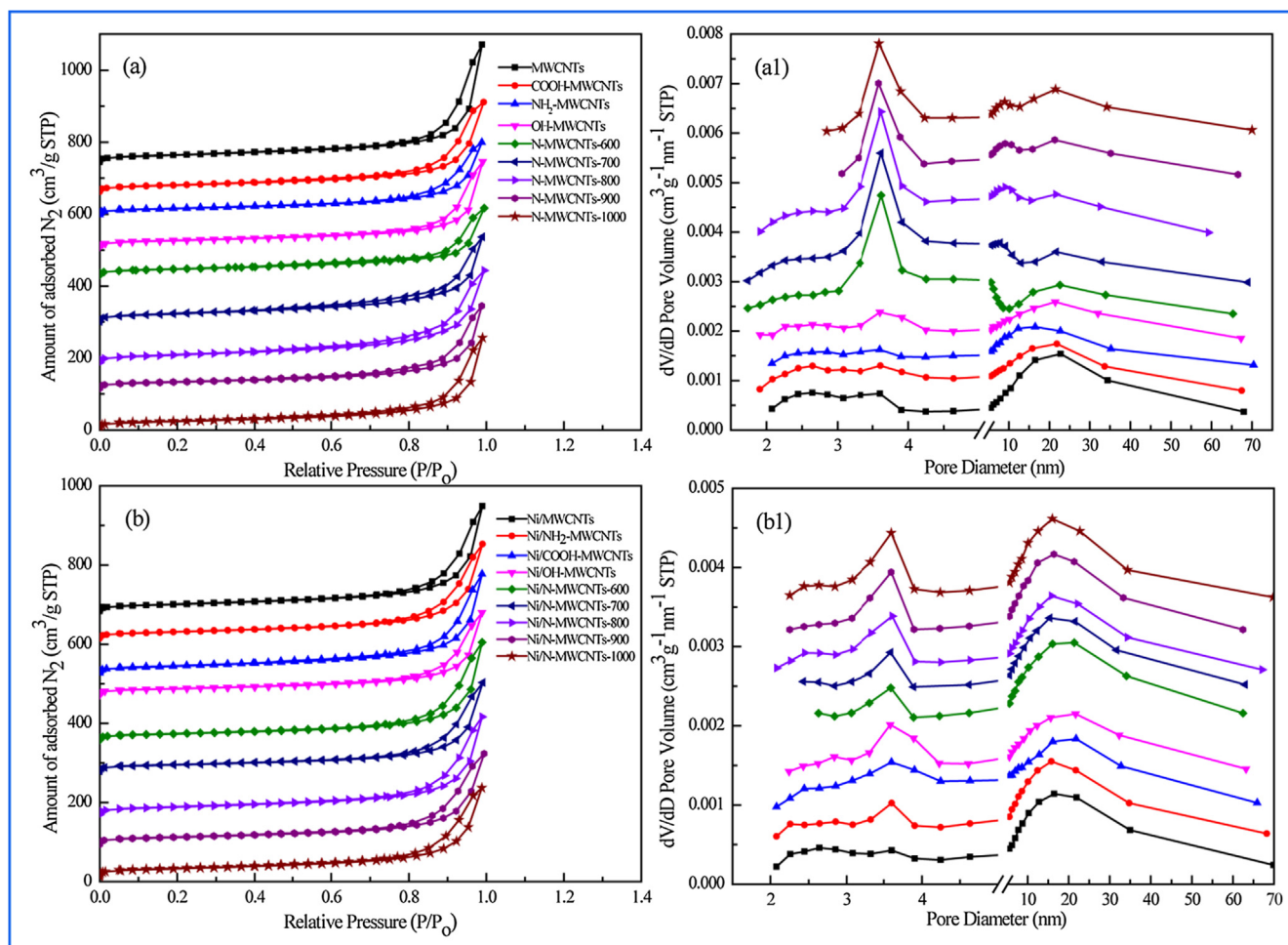
Fig. 1. N_2 adsorption-desorption isotherms (a, b) and BJH pore size distribution (a1, b1) of the samples.

$1345\ cm^{-1}$, $1585\ cm^{-1}$ and $2600\ cm^{-1}$ are ascribed to the D-band, G-band and 2D-band in all the samples [42,43]. The D-band is ascribed to the vibration of A_{1g} breathing associated with the presence of defects and disorders in sp3-hybridized carbon atoms, and the G-band is attributed to E_{2g} tangential vibrations related to sp2-hybridized carbon atoms in graphite layer [42,43]. In addition, the 2D-band is originated from the double resonance Raman process concerned with two phonons with opposite momentum. In general, the disorder degrees of MWCNTs are measured by the intensity ratio of D-band peak to G-band peak (I_D/I_G). As seen in Fig. 3-1, the value of I_D/I_G increases with the introduction of functional group and N species, indicating that the surface defects of MWCNTs increase. It has been found that introduction of functional group such as NH_2—, COOH— and OH— on the surface of MWCNTs *via* chemical covalent action can obviously increase the value of I_D/I_G as well as the surface defects [44,45]. Typically, N-MWCNTs-800 (Fig. 3-1-g) presents the highest I_D/I_G value (1.43). And the intensity of 2D-band in N-MWCNTs-800 (Fig. 3-1-g) is weaker than others, further testify the existence of more defect sites [43]. Moreover, it can be seen that the D-band and G-band in N-MWCNTs shift slightly to higher wave numbers. It is believed that the D-band shift is ascribed to the change of the six-member-ring structure by doping of heteroatoms, while the G-band shift is caused by C-C expansion and electronic structure changes that N species can serve as either electron acceptor or donor [42]. Additionally, as shown in Fig. 3-2, all the supported Ni-based catalysts exhibit the relatively lower I_D/I_G values than the support, the rea-

son may that the nanoparticles prefer to anchor on the structural defect sites on the surface of MWCNTs during the loading process [39]. Hence, the functionalized MWCNTs with more defect sites may have smaller and better dispersed Ni nanoparticles.

3.1.4. H_2-TPR

The H_2-TPR profiles of the samples are shown in Fig. 4. It can be seen from Fig. 4 that all the samples present two distinct broad hydrogen consumption peaks, the former peak around 650 K is ascribed to the reduction of nickel oxide, and the latter peak is attributed to methanation of MWCNTs in hydrogen atmosphere under high temperature [38,46]. Noticeably, the reduction peck of NiO in functional group (NH_2, COOH and OH) modified MWCNTs shift to lower temperature, suggesting that the functional group such as NH_2, COOH and OH can effectively affect the Ni nanoparticles nucleation rate so as to decrease the reduction activation energy of NiO [29,30]. What's more, the intensity of NiO reduction peaks in these samples increase in the following order: NiO/MWCNTs < NiO/NH_2-MWCNTs < NiO/COOH-MWCNTs < NiO/OH-MWCNTs, suggesting that more active centers are formed in NiO/OH-MWCNTs under same reduction conditions. It is generally accepted that metal oxides in a highly dispersed state with smaller crystallite size present lower reduction activation energy [28]. Consequently, highly dispersed and small NiO nanoparticles may form in these functional group modified MWCNTs. Additionally, it can be seen from Fig. 4 that the reduction peak of NiO in N species modified MWCNTs under different pyrolysis temperature

Table 1
Textural property of different catalysts.

Catalysts	BET surface area (m^2g^{-1})	Average pore diameter (nm)	Pore volume (cm^3g^{-1})
MWCNTs	76.8	16.9	0.34
NH_2-MWCNTs	79.8	18.3	0.37
COOH-MWCNTs	82.5	17.9	0.39
OH-MWCNTs	81.6	18.1	0.36
N-MWCNTs-600	75.0	15.8	0.34
N-MWCNTs-700	94.4	14.7	0.37
N-MWCNTs-800	96.4	15.5	0.40
N-MWCNTs-900	75.9	18.6	0.36
N-MWCNTs-1000	76.3	19.8	0.38
Ni/MWCNTs	67.8	21.1	0.30
Ni/NH_2-MWCNTs	70.2	20.0	0.35
Ni/COOH-MWCNTs	73.9	18.9	0.37
Ni/OH-MWCNTs	68.9	20.6	0.32
Ni/N-MWCNTs-600	70.9	20.8	0.31
Ni/N-MWCNTs-700	83.7	19.5	0.35
Ni/N-MWCNTs-800	85.1	18.6	0.34
Ni/N-MWCNTs-900	70.9	21.3	0.34
Ni/N-MWCNTs-1000	71.5	19.9	0.35

Fig. 3. Raman spectra of the MWCNTs (1-a), NH_2-MWCNTs (1-b), COOH-MWCNTs (1-c), OH-MWCNTs (1-d), N-MWCNTs-600 (1-e), N-MWCNTs-700 (1-f), N-MWCNTs-800 (1-g), N-MWCNTs-900 (1-h), N-MWCNTs-1000 (1-i), Ni/MWCNTs (2-a), Ni/NH_2-MWCNTs (2-b), Ni/COOH-MWCNTs (2-c), Ni/OH-MWCNTs (2-d), Ni/N-MWCNTs-600 (2-e), Ni/N-MWCNTs-700 (2-f), Ni/N-MWCNTs-800 (2-g), Ni/N-MWCNTs-900 (2-h) and Ni/N-MWCNTs-1000 (2-i).
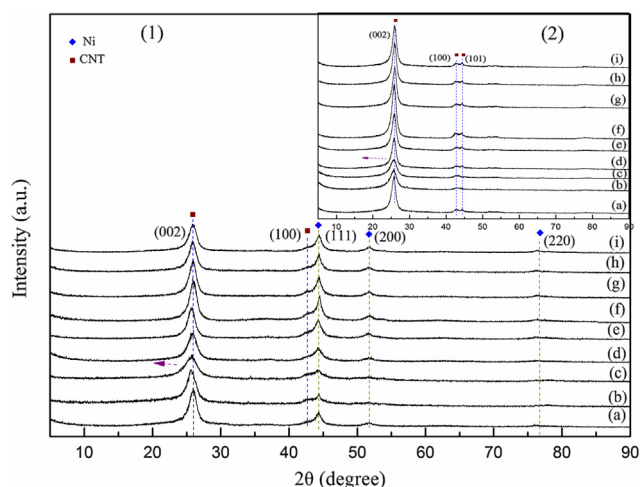

Fig. 2. XRD patterns of the Ni/N-MWCNTs-600 (1-a), Ni/N-MWCNTs-700 (1-b), Ni/N-MWCNTs-800 (1-c), Ni/N-MWCNTs-900 (1-d), Ni/N-MWCNTs-1000 (1-e), Ni/MWCNTs (1-f), Ni/NH_2-MWCNTs (1-g), Ni/COOH-MWCNTs (1-h), Ni/OH-MWCNTs (1-i), N-MWCNTs-600 (2-a), N-MWCNTs-700 (2-b), N-MWCNTs-800 (2-c), N-MWCNTs-900 (2-d), N-MWCNTs-1000 (2-e), MWCNTs (2-f), NH_2-MWCNTs (2-g), COOH-MWCNTs (2-h) and OH-MWCNTs (2-i).

Fig. 4. H_2-TPR profiles of the NiO/MWCNTs (a), NiO/NH_2-MWCNTs (b), NiO/COOH-MWCNTs (c), NiO/OH-MWCNTs (d), NiO/N-MWCNTs-600 (e), NiO/N-MWCNTs-700 (f), NiO/N-MWCNTs-800 (g), NiO/N-MWCNTs-900 (h) and NiO/N-MWCNTs-1000 (i).

decreases to 615 K with the pyrolysis temperature increasing from 873 K to 1073 K, and then increases to 655 K with the pyrolysis temperature increasing from 1073 K to 1273 K. The reason may be that nitrogen content and nitrogen species type are affected by pyrolysis temperature, which further affect the reduction activation energy and reduction degree of NiO [28,31,32]. Moreover, it is worthwhile to note that NiO/N-MWCNTs-800 shows the lowest reduction activation energy and the strongest reduction peak strength, it indicates that introduction of N species under pyrolysis temperature of 1073 K presents the best dispersion and the smallest NiO nanoparticles, and thus form the maximum active metallic Ni [28,31,32].

3.1.5. SEM

Fig. 5 shows the morphology of the pristine MWCNTs and functionalized MWCNTs. It can be seen from Fig. 5(a) that the pristine MWCNTs are cluttered and tightly wound together, however, the functional group such as COOH—, OH— and NH_2— modified MWCNTs in Fig. 5(b–d) show that looser network structures form along with more opened gaps (seeing from arrow direction). N-
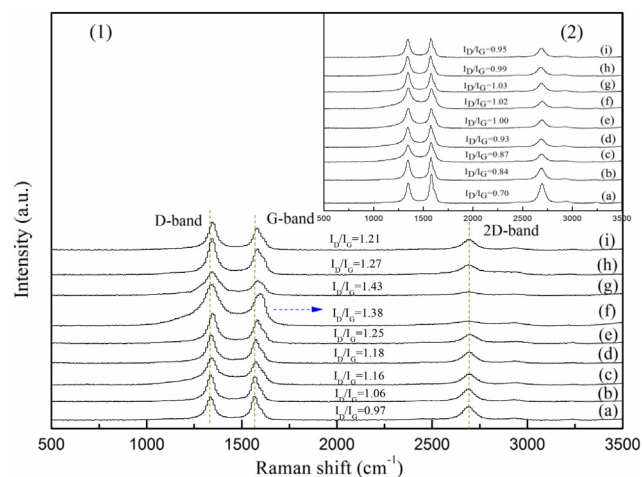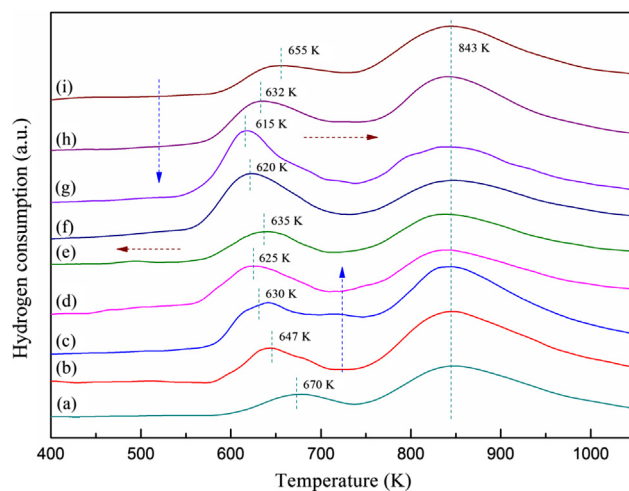
MWCNTs-800 in Fig. 5(e, f) presents shorter and finer MWCNTs (Fig. 5(e)), and local magnification of Fig. 5(e) shows more sunken, fold shaded parts on the surface of MWCNTs (Fig. 5(f)), it indicates that more defect sites are formed. The typical SEM micrographs of MWCNTs and functionalized MWCNTs supported catalysts are shown in Fig. 6. Ni nanoparticles in Ni/MWCNTs present obvious aggregation, this phenomenon also appeared in our previous studies [22]. On the contrary, the functional group and N species modified MWCNTs possess more uniform and better dispersed Ni nanoparticles, the reason may that the functional group such as COOH—, OH— and NH_2— act on Ni ions *via* electrostatic attractions and chemical interactions so as to provide nucleation centers, and N species modified MWCNTs is due to the strong synergistic effect between N species and Ni nanoparticles. Typically, Ni/N-MWCNTs-800 (Fig. 6(e, e1)) shows better dispersed, more uniform and smaller Ni nanoparticles, and local magnification of Fig. 6(e) shows that the size of Ni nanoparticles is approximately close to 3–4 nm (Fig. 6(e1)).
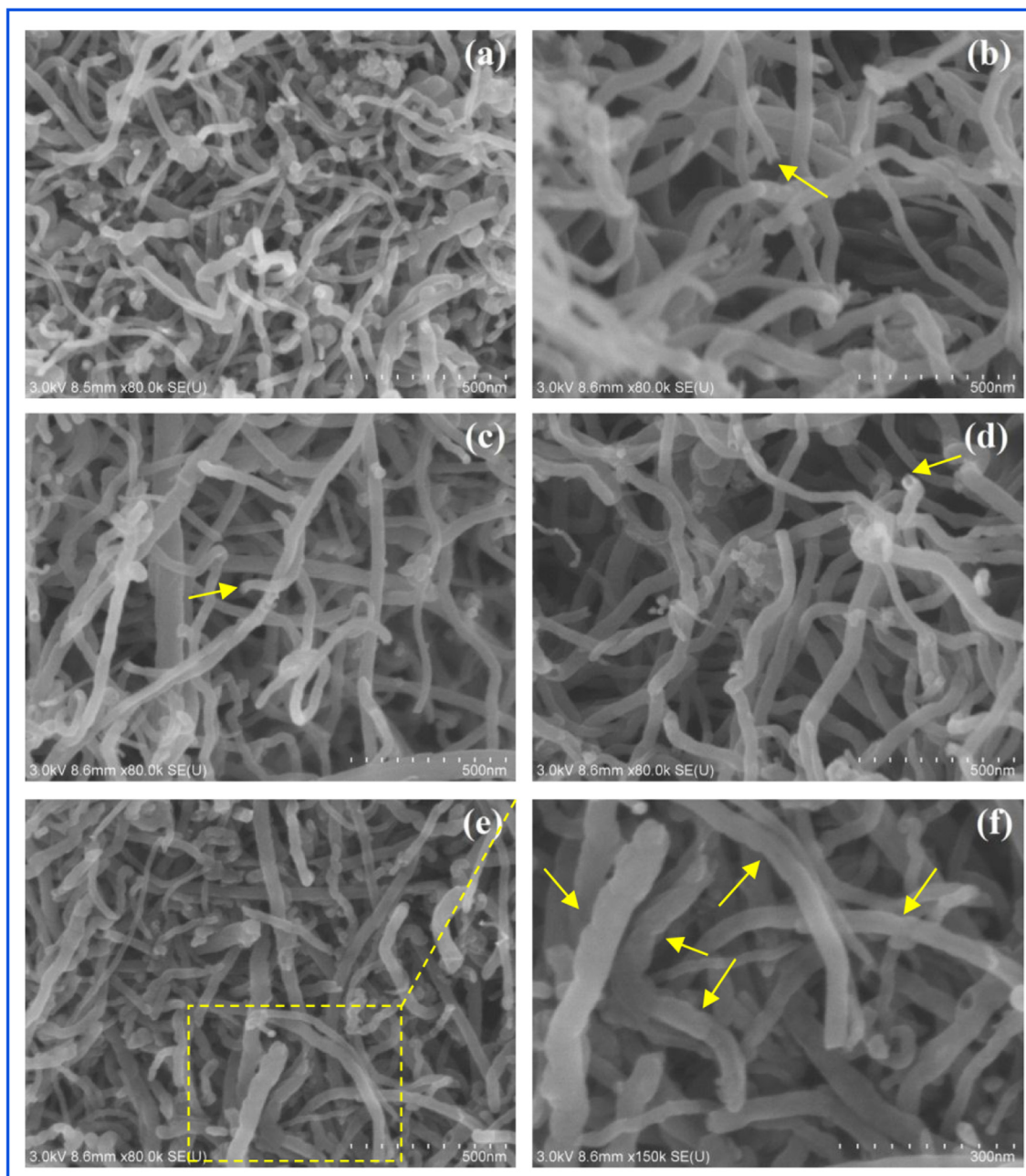
Fig. 5. SEM images of pristine MWCNTs (a), COOH-MWCNTs (b), OH-MWCNTs (c), NH$_2$-MWCNTs (d) and N-MWCNTs-800 (e, f).

3.1.6. FT-IR spectrum

Fig. 7 presents the FT-IR spectrum of the samples. As shown in Fig. 7-1, there are four obvious stretching vibration peaks at 3452 cm^{-1}, 1641 cm^{-1}, 1390 cm^{-1} and 1060 cm^{-1}, which are ascribed to O—H, C≡C, C—O—H and C—O(H) stretching respectively [47–50]. The O—H peak at 3452 cm^{-1} is originated from isolated surface —OH in hydroxyl groups and/or —OH in carboxyl groups as well as absorbed water on MWCNTs [47–50]. Moreover, the peaks at 1390 cm^{-1} and 1060 cm^{-1} are ascribed to C—O—H bending vibration and C—O(H) stretching vibration [47,49,50]. Meanwhile, weak vibration bands at 2835 cm^{-1} and 2920 cm^{-1} are due to the stretching vibration of sp^3 C—H and sp^2 C—H [50]. Differing from MWCNTs, the spectrum of COOH-MWCNTs in Fig. 7-1-c possess stronger intensity of O—H group at 3452 cm^{-1}, 1390 cm^{-1} and 1060 cm^{-1}, suggesting that more oxygenated functional groups exist on the surface of COOH-MWCNTs. Furthermore,

typical stretching vibration peaks appear at 1457 cm^{-1}, 1560 cm^{-1} and 1745 cm^{-1}, the first two peaks represent the symmetric and asymmetric stretching vibration of —COO— [50,51], and the latter is assigned to C=O stretching in carboxyl groups [48–51]. In addition, the broadest sharp vibration peaks at 3452 cm^{-1}, 1390 cm^{-1} and 1060 cm^{-1} imply that a large number of O—H have been introduced onto OH-MWCNTs (Fig. 7-1-b) [47–50]. And the FT-IR spectrum of the NH$_2$-MWCNTs is shown in Fig. 7-1-a, a broader peak at 3452 cm^{-1} may due to the introduction of N—H, which may be coupled with O—H vibration [48,50]. In addition, the peaks at 1160 cm^{-1} and 845 cm^{-1} are ascribed to the stretching vibration of N—H [48,50] and —NH$_2$ stretching vibration [48], which is further identified that the amine group is successfully introduced.

Fig. 7-2 illustrates the FT-IR spectra of N functionalized MWCNTs under different pyrolysis temperature, and the doped N species has significantly influence on the chemical structure of
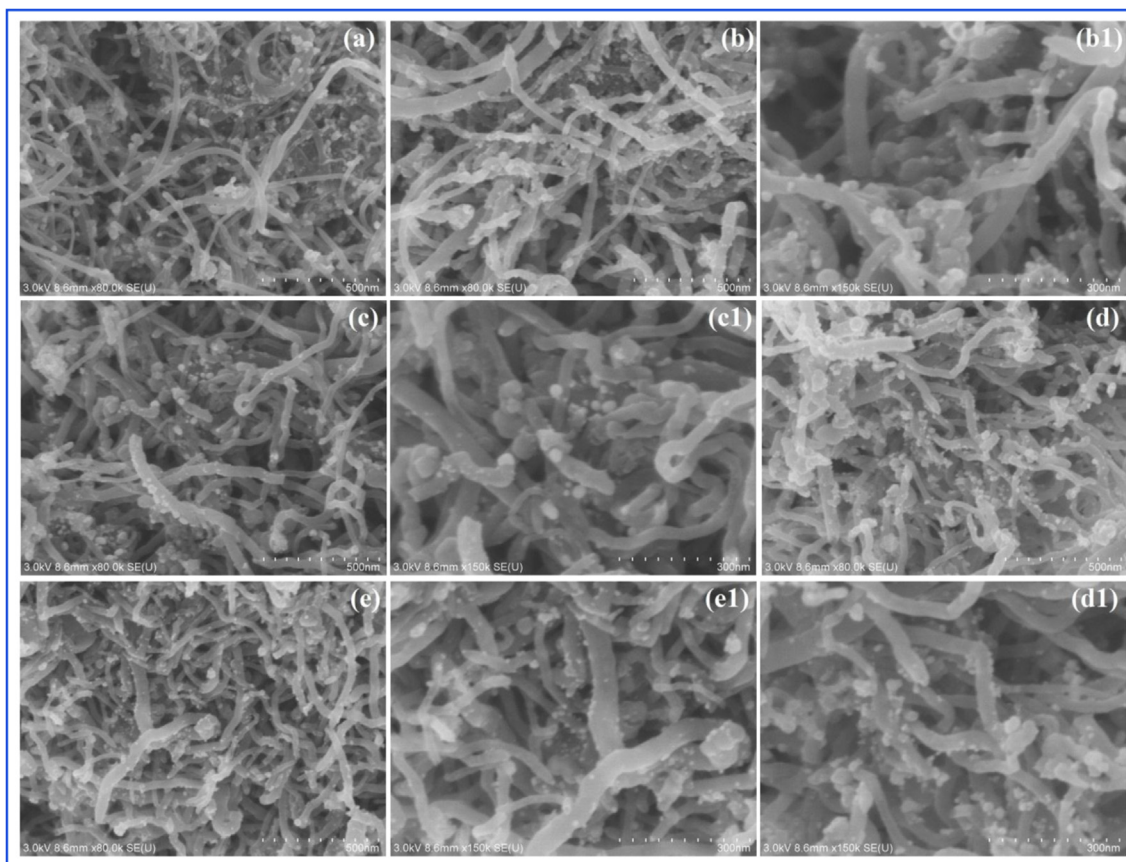
Fig. 6. SEM images of Ni/MWCNTs (a), Ni/COOH-MWCNTs (b, b1), Ni/NH$_2$-MWCNTs (c, c1), Ni/OH-MWCNTs (d, d1) and Ni/N-MWCNTs-800 (e, e1).
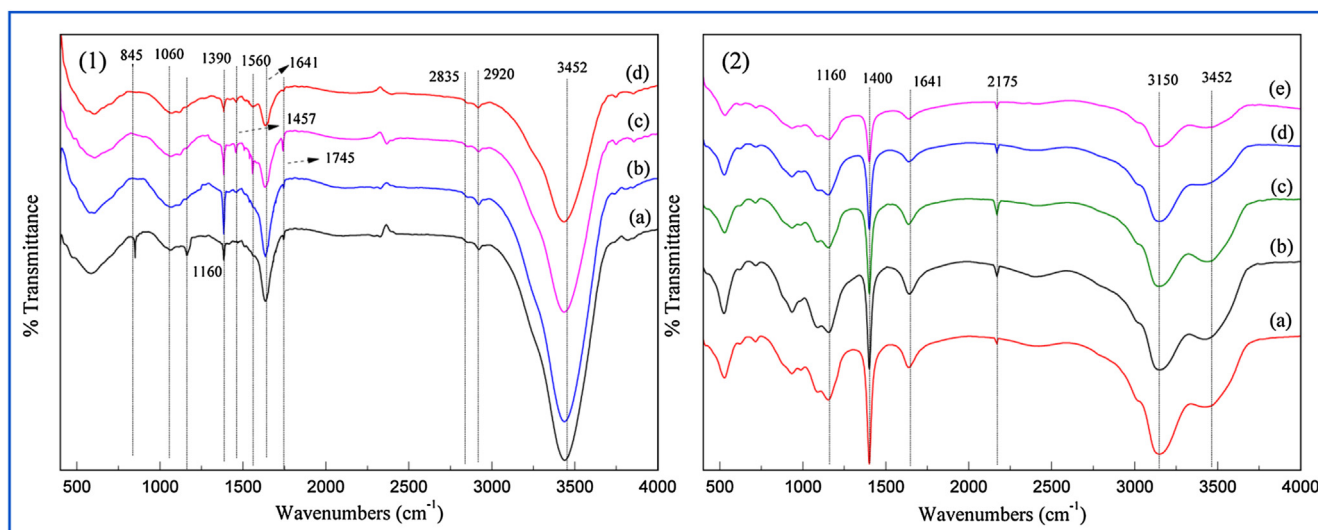

Fig. 7. FT-IR spectrum of the NH$_2$-MWCNTs (1-a), OH-MWCNTs (1-b), COOH-MWCNTs (1-c), MWCNTs (1-d), N-MWCNTs-600 (2-a), N-MWCNTs-700 (2-b), N-MWCNTs-800 (2-c), N-MWCNTs-900 (2-d), N-MWCNTs-1000 (2-e).

MWCNTs. As shown in Fig. 7-2, four typical vibrational peaks at 3150 cm^{-1}, 2175 cm^{-1}, 1400 cm^{-1} and 1160 cm^{-1} appear in all the samples [25,52,53]. The peak at 3150 cm^{-1} is the stretching vibration of N-H, while the band at 1160 cm^{-1} and 1400 cm^{-1} are stretching vibration of C-N, in which the former is ring stretching and the latter is coupled with C—O stretching vibration [52,53]. Moreover, a small weak vibrational peak at 2175 cm^{-1} is assigned to the —C≡N symmetric stretching vibration [52], and it becomes

the strongest in N-MWCNTs-800 (Fig. 7-2-c), the reason may that too high or two low temperature is not good at nitrogen doping. And it can be seen that the intensity of C—N stretching vibration peaks at 1160 cm^{-1} and 1400 cm^{-1} gradually become weaker with the increment of pyrolysis temperature, which indicates that melamine formaldehyde resin is decomposed quickly with the temperature. Furthermore, the wide vibration peaks in the range of 400–900 cm^{-1} can be attributed to the out-of-plane bending vibrations

of graphite-like sp2 domains, which can get a response from the FT-IR spectra due to that N incorporated into the bonding network [53].

3.1.7. XPS

Fig. 8 shows the C 1s and O 1s XPS patterns of MWCNTs, COOH-MWCNTs and OH-MWCNTs. The C1s peak can be deconvoluted into six Gaussian peaks: sp2-hybridized C=C (284.5 eV), sp3-hybridized C—C (285.3 eV), C—OH (286.3 eV), C=O (287.5 eV), COOH (288.9 eV) and $\pi-\pi^*$ transition loss peak (291.1 eV) [26,54,55], meanwhile, the three Gaussian fitted peaks at 531.4 eV, 532.6 eV and 534.4 eV in O 1s spectrum are assigned to C=O, C—OH and COOH respectively [26,55]. It is obvious that the C 1s pattern of COOH-MWCNTs (Fig. 8(b)) presents stronger peak intensity of C=O, C—OH and COOH than MWCNTs, besides, the peak intensity of C=O and COOH in O 1s spectrum (Fig. 8(b1)) also become strong, indicating that abundant of oxygen functional group such as C=O, C—OH and COOH are introduced, especially C=O and COOH. Additionally, for C 1s spectrum of OH-MWCNTs in Fig. 8(c), it shows that C—OH and C=O increase in intensity while COOH bond has little change, moreover, O 1s spectrum of OH-MWCNTs presents the highest peak intensity of C—OH in Fig. 8(c1), suggesting that large number of OH have been decorated on OH-MWCNTs. Therefore, obvious variations in the peak intensity evidently suggest that more OH exist on OH-MWCNTs, while more COOH are attached on COOH-MWCNTs, these results are consistent with FT-IR characterization in Fig. 7.

Furthermore, N 1s XPS patterns of NH2-MWCNTs and N functionalized MWCNTs are presented in Fig. 9. As shown in Fig. 9(a), there is only one peak at 399.6 eV, which is ascribed to N species in NH2 groups, suggesting that NH2 groups are successfully introduced [56], this is in agreement with the FT-IR characterization in Fig. 7(a). Besides, the N 1s XPS patterns of N functionalized MWCNTs in Fig. 9(b)–(f) can be fitted into four peaks at 398.4 eV, 400.0 eV, 401.4 eV and 402.9 eV, which are ascribed to pyridinic N, pyrrolic N, graphitic N and oxide N respectively [27,28,57,58]. And the content and state of nitrogen in N-doped MWCNTs are summarized in Table 2. As shown in Fig. 9, with the increment of pyrolysis temperature, the peak intensity of different nitrogen varies significantly, indicating that temperature is the main factor that affects the active sites of nitrogen. Moreover, it can be seen from Table 2 that the N content decreases rapidly from 16.68% (N-MWCNTs-600) to 3.21% (N-MWCNTs-1000), since C-N is easy to break at high temperature [59]. Graphitic N increases continuously with the pyrolysis temperature, while pyridinic N increases first and then declines, the reason is due to that low thermal stability of pyridinic N and pyrrolic N is quite easy to convert into graphitic N at high temperature [59]. Notably, N-MWCNTs-800 possesses the highest content ratio of pyridinic N. Many researchers found that pyridinic N can be acted as the main active site for stabilization of metal or oxide particles on the support surface and thus affect the nanoparticles size, electronic valence state and catalytic performance [27,28,57,58]. And more importantly, pyridinic N is generally considered as the main metal-binding site for transition-metal species in N-doped carbon catalyst [58,60]. Especially, Liu et al. constructed the coordination model of isolated nickel ion with the adjoining non-coordinated pyridinic N atoms, in which (Ni—N4)⋯N structure possesses high activity and ultra-stability in Ni—N—C catalyst and serve as main active site for various unsaturated substrates hydrogenation [58].

Fig. 10 presents Ni 2p$_{3/2}$ XPS patterns of the samples. Ni 2p$_{3/2}$ spectra can be fitted into three components, the peak around 852.8 eV, 854.5 eV and 856.4 eV are ascribed to Ni^{0+}, Ni^{2+} and Ni^{3+} respectively [61]. In addition, there is a broad peak at high binding energy of 861.7 eV, which is assigned to the shake-up satellite accompanied by high valence nickel [62]. As shown in

Fig. 10, Ni/MWCNTs exhibit the lowest peak intensity of Ni^{0+} in comparison with other samples, while the functional group modified MWCNTs supported catalysts display higher peak intensity of Ni^{0+}, suggesting that functional group can effectively act on metal ions by electrostatic attractions and chemical interactions so as to provide nucleation sites, and thus enhance the reduction degree of NiO as well as obtain higher proportion of metallic Ni [29,30]. Similarly, as can be seen in N doped MWCNTs in Fig. 10, the stronger peak intensity of Ni^{0+} than Ni/MWCNT is presented, indicating that the introduction of N species can effectively boost the reduction of NiO so as to increase the percentage of Ni^{0+}. And the fact that the metallic Ni content can be increased by doping N species has also identified by many researchers [28,31,57,63]. Also, the surface compositions of the samples are displayed in Table 3. As shown in Table 3, the content of Ni^{0+} in N doped MWCNTs increases firstly and then decreases when the pyrolysis temperature increases from 873 K to 1273 K, and Ni/N-MWCNTs-800 possesses the highest Ni^{0+} content. Moreover, pyridinic N is considered as metal-binding sites for transition-metal [58,60] and active site for promoting NiO reduction [27,28,57], it also can be seen that Ni/N-MWCNTs-800 presents the highest pyridinic N ratio. Additionally, it can be seen in Table 3 that the binding energy of Ni species shifts toward higher value with the increment pyridinic N ratio, the reason may be that the pyridinic N can effectively influence on the electronic structure of Ni species due to the electron transfer between Ni and N species. Ning et al. found that pyridinic N can serve as electron-acceptor and thus result in higher binging energy of Pt/NCNTs (H2) than other samples [64]. Nevertheless, the influence of size effect on the electronic structure of metal cannot be ignored since smaller metal nanoparticles would present higher binging energy [64,65]. Hence, Ni/N-MWCNTs-800 may possess smaller Ni nanoparticles in comparison with other samples.

3.1.8. TEM

The HAADF-STEM images of functional group modified MWCNTs and their corresponding elemental mappings are presented in Fig. 11. As shown in Fig. 11, COOH-MWCNTs (Fig. 11(b)) and OH-MWCNTs (Fig. 11(c)) possess high strength of oxygen element, while the distribution of oxygen elements for MWCNTs (Fig. 11(a)) is hardly detectable, intuitively proves that oxygen functional groups such as COOH and OH have been introduced. In addition, the HAADF-STEM images of NH2-MWCNTs in Fig. 11(d) present the distribution of C, O and N, here N is undeniable originated from NH2, further suggests that the NH2 group exists in the surface of NH2-MWCNTs. The results are consistent with the FT-IR in Fig. 7 and XPS in Fig. 8. And Fig. 12 illustrates the selected TEM images of representative catalysts and their corresponding histograms of nanoparticles distribution. As shown in Fig. 12(a), there is exist heterogeneous and heavy aggregation for Ni nanoparticles owing to sintering during the reduction process, therefore we can see large span Ni nanoparticles distribution of 6 nm to 22 nm in Fig. 12(a2), and mainly centered around 10 nm. Conversely, the TEM images of functional group modified MWCNT supported catalysts (Fig. 12(b)–(d)) show good dispersion and narrow size distribution of Ni nanoparticles, especially for Ni/OH-MWCNTs, the reason may be that these functional group can serve as anchoring sites for Ni species by electrostatic attractions and chemical interactions accompanied with providing the nucleation site, thereby promoting the Ni nanoparticles distribution [26,29–31,33,44,58]. Moreover, Ni/N-MWCNTs-800 (Fig. 12(e) and (e2)) shows the best dispersion of Ni nanoparticles with the narrowest size distribution mainly centered around 2–3 nm, the reason may be that large amount of defects formed by doping N species and the strong electronic interactions between nitrogen species and Ni can effectively stabilize the nanoparticles, and thus promote to form ultra-small particles and enhance the dispersion
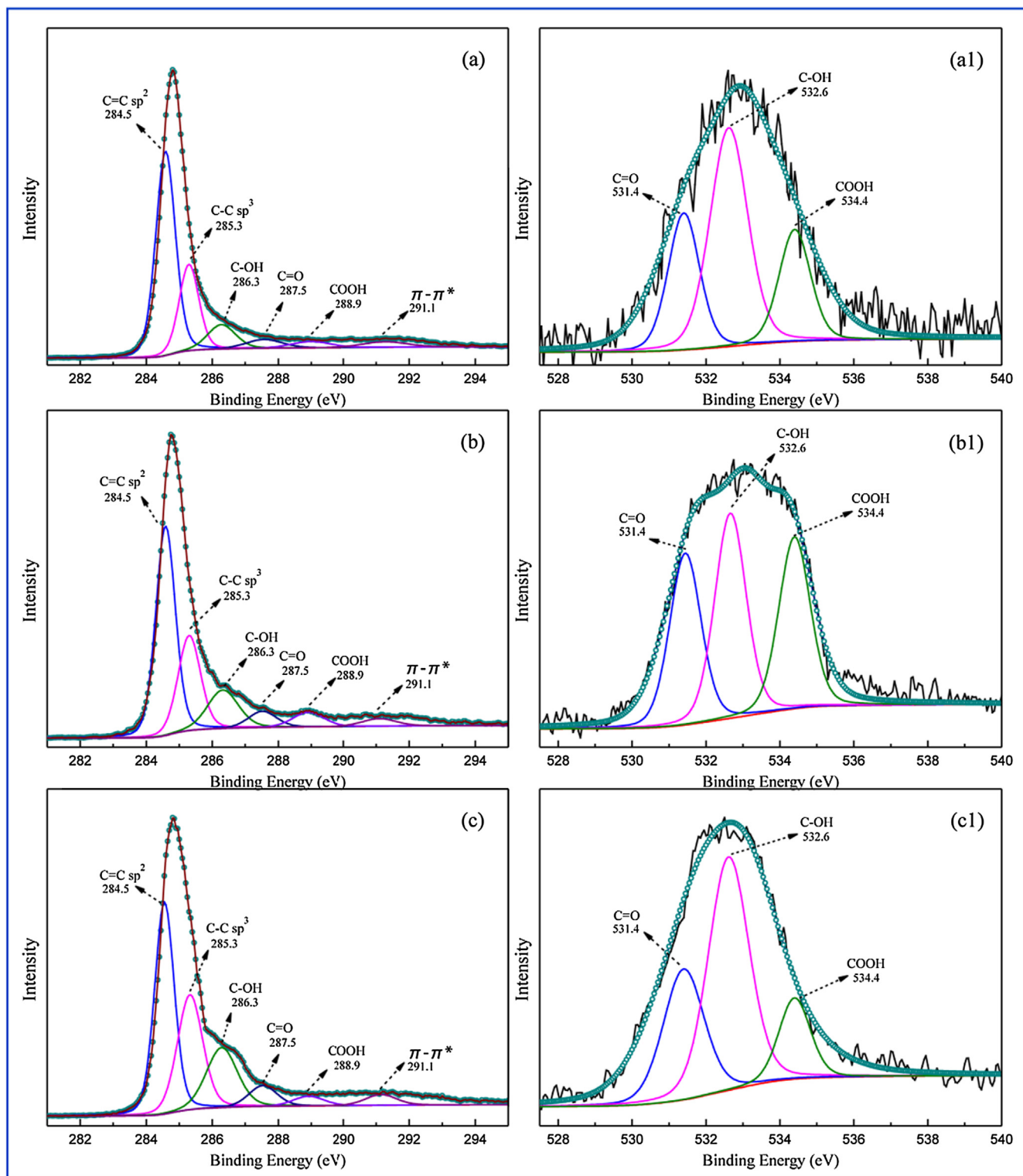
Fig. 8. C 1s XPS patterns of MWCNTs (a), COOH-MWCNTs (b), OH-MWCNTs (c) and O 1s XPS patterns of MWCNTs (a1), COOH-MWCNTs (b1), OH-MWCNTs (c1).

[27,28,31,57,63,65]. Additionally, as can be seen in Fig. 12(f), Ni/N-MWCNTs-1000 again appears a certain degree of agglomeration, the reason may due to that high pyrolysis temperature leads to low nitrogen content and graphitized carbon surface, which is not helpful to the stabilization of Ni nanoparticles and its dispersion. These results agree with the characterization results of XRD, Raman spectra and H_2-TPR in Figs. 2–4. Furthermore, HAADF-

STEM image of Ni/N-MWCNTs-800 and their corresponding elemental mappings are shown in Fig. 12(g) and (g1-4), suggesting that the well-distributed C, O, N and Ni.

3.1.9. H_2 chemisorption

Table 4 shows the H_2 chemisorption data. It can be seen from Table 4 that the functional group modified catalysts possess higher
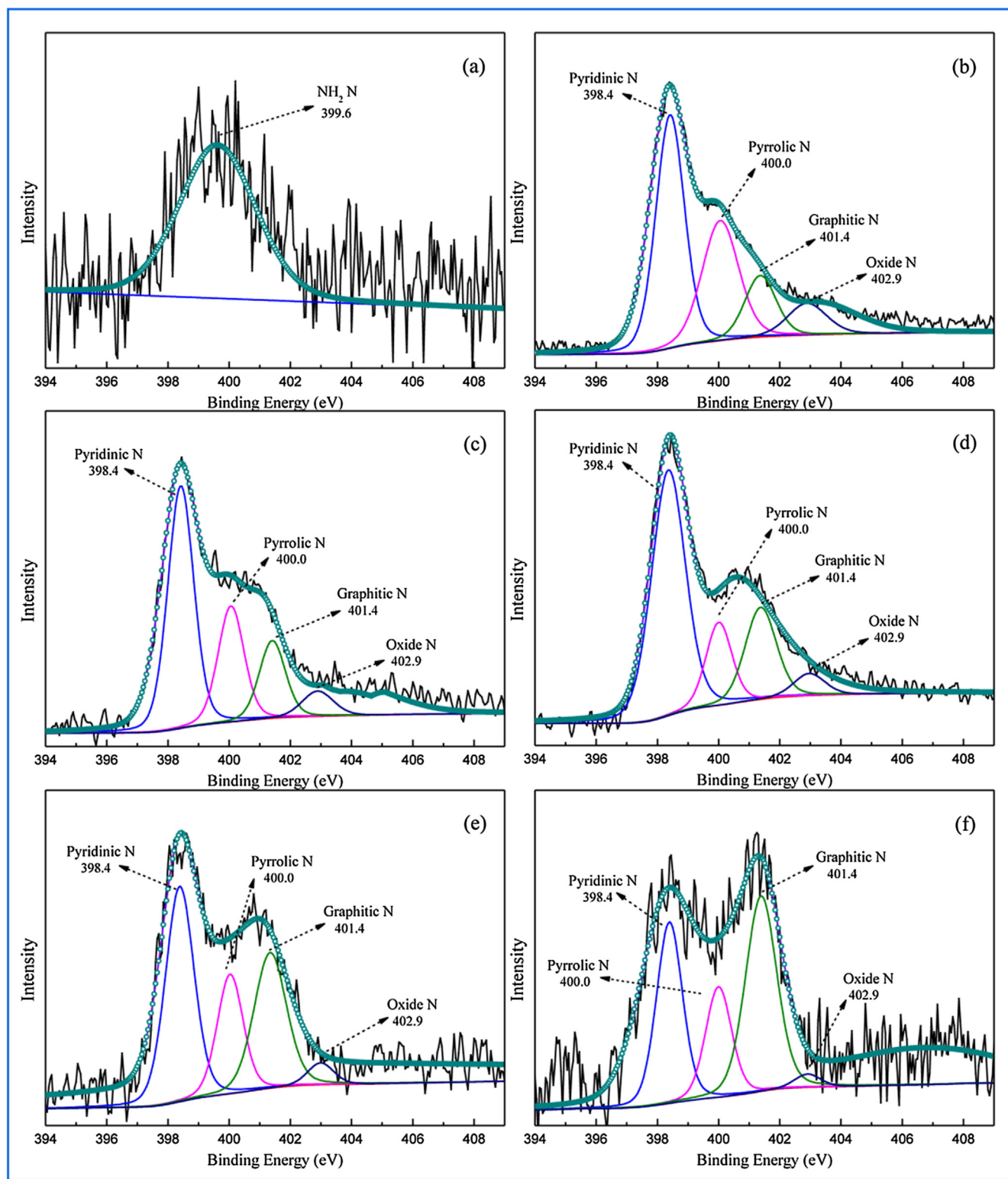
Fig. 9. N 1s XPS patterns of NH_2-MWCNTs (a), N-MWCNTs-600 (b), N-MWCNTs-700 (c), N-MWCNTs-800 (d), N-MWCNTs-900 (e) and N-MWCNTs-1000 (f).

values of H_2 uptake quantity, metallic surface areas and better metallic dispersion, the reason may be due to the dispersion of Ni nanoparticles can be enhanced by introduction of functional group, and thus decreases the reduction activation energy of NiO [29,30]. Similarly, N species modified catalysts also present higher H_2 chemisorption values, which is due to the formation of highly

dispersed Ni nanoparticles by N doping [28,31,32]. Noticeably, Ni/N-MWCNTs-800 shows the highest H_2 uptake quantity of 139.32 $\mu L\,g^{-1}$, metallic Ni surface area of 0.83 $m^2\,g^{-1}$ and metallic dispersion of 8.56%. And the results obtained by H_2 chemisorption are in good agreement with the H_2-TPR in Fig. 4, XPS in Fig. 10 and TEM in Fig. 12.

Table 2
The content and state of nitrogen in N-doped MWCNTs under different temperature.[a]

Samples	N content (%)	N_P (%)	N_{Pyr} (%)	N_G (%)	NO_X (%)
N-MWCNTs-600	16.68	47.03	30.75	13.50	8.72
N-MWCNTs-700	13.21	54.01	23.86	15.63	6.50
N-MWCNTs-800	10.52	59.28	15.39	20.44	4.89
N-MWCNTs-900	6.62	43.28	21.80	30.94	3.98
N-MWCNTs-1000	3.21	33.62	20.48	43.46	2.44

[a] N_P: Pyridinic N, N_{Pyr}: Pyrrolic N, N_G: Graphitic N, NO_X: Oxide N.
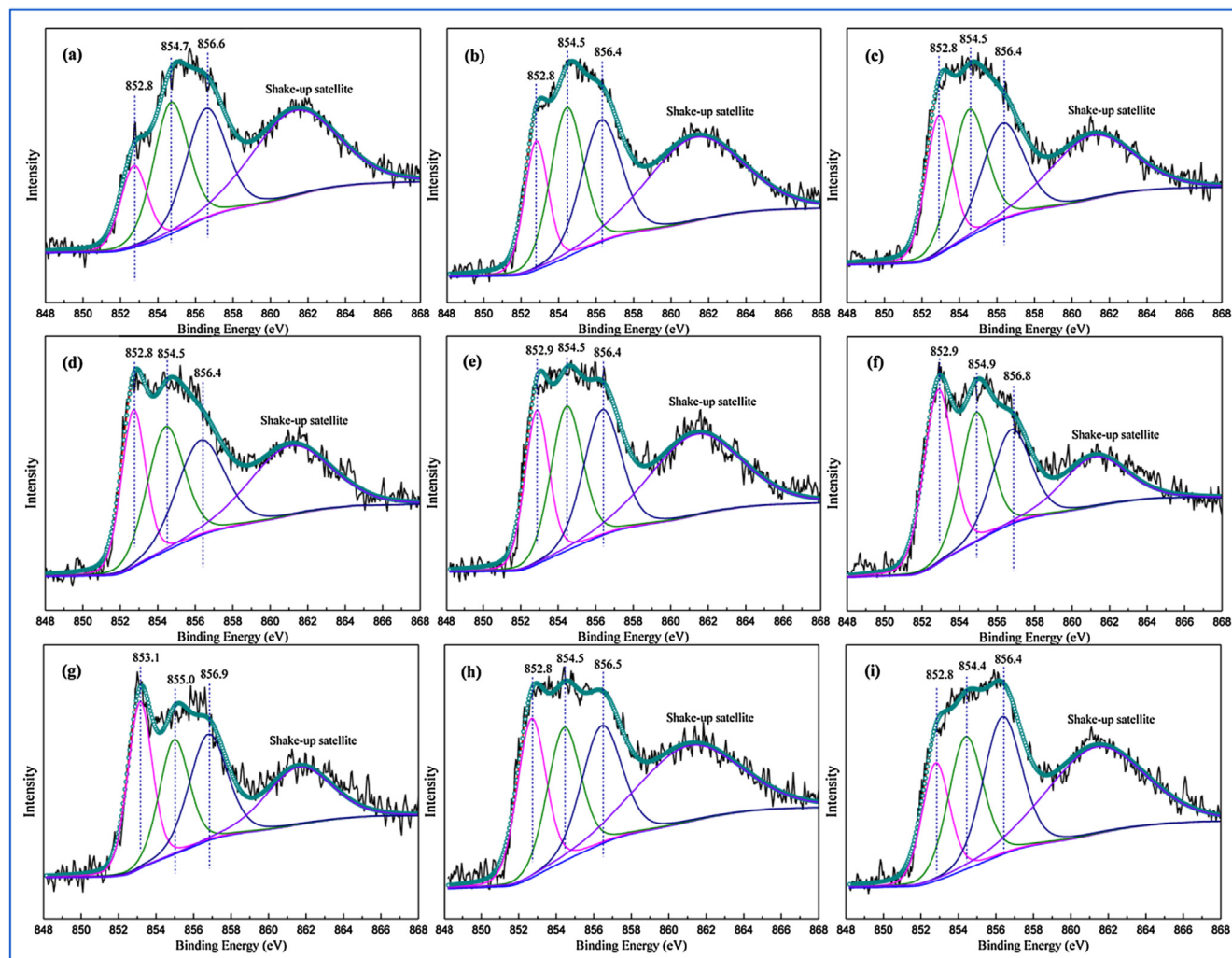
Fig. 10. Ni $2p_{3/2}$ XPS patterns of Ni/MWCNTs (a), Ni/NH$_2$-MWCNTs (b), Ni/COOH-MWCNTs (c), Ni/OH-MWCNTs (d), Ni/N-MWCNTs-600 (e), Ni/N-MWCNTs-700 (f), Ni/N-MWCNTs-800 (g), Ni/N-MWCNTs-900 (h) and Ni/N-MWCNTs-1000 (i).

Table 3
Surface compositions of the different MWCNT supported nickel catalysts.

| Catalysts	Binding energy (eV)			Peak area ratio (%)		
	Ni^{0+}	Ni^{2+}	Ni^{3+}	Ni^{0+}	Ni^{2+}	Ni^{3+}
Ni/MWCNT	852.8	854.7	856.6	19.73	41.05	39.22
Ni/NH$_2$-MWCNTs	852.8	854.5	856.4	24.94	37.27	37.79
Ni/COOH-MWCNTs	852.8	854.5	856.4	27.80	37.53	34.67
Ni/OH-MWCNTs	852.8	854.5	856.4	29.60	35.51	34.89
Ni/N-MWCNTs-600	852.9	854.5	856.4	28.51	35.20	36.29
Ni/N-MWCNTs-700	852.9	854.9	856.8	37.84	32.31	29.85
Ni/N-MWCNTs-800	853.1	855.0	856.9	39.33	28.56	32.11
Ni/N-MWCNTs-900	852.8	854.5	856.5	33.24	32.31	34.45
Ni/N-MWCNTs-1000	852.8	854.4	856.4	24.91	34.80	40.29
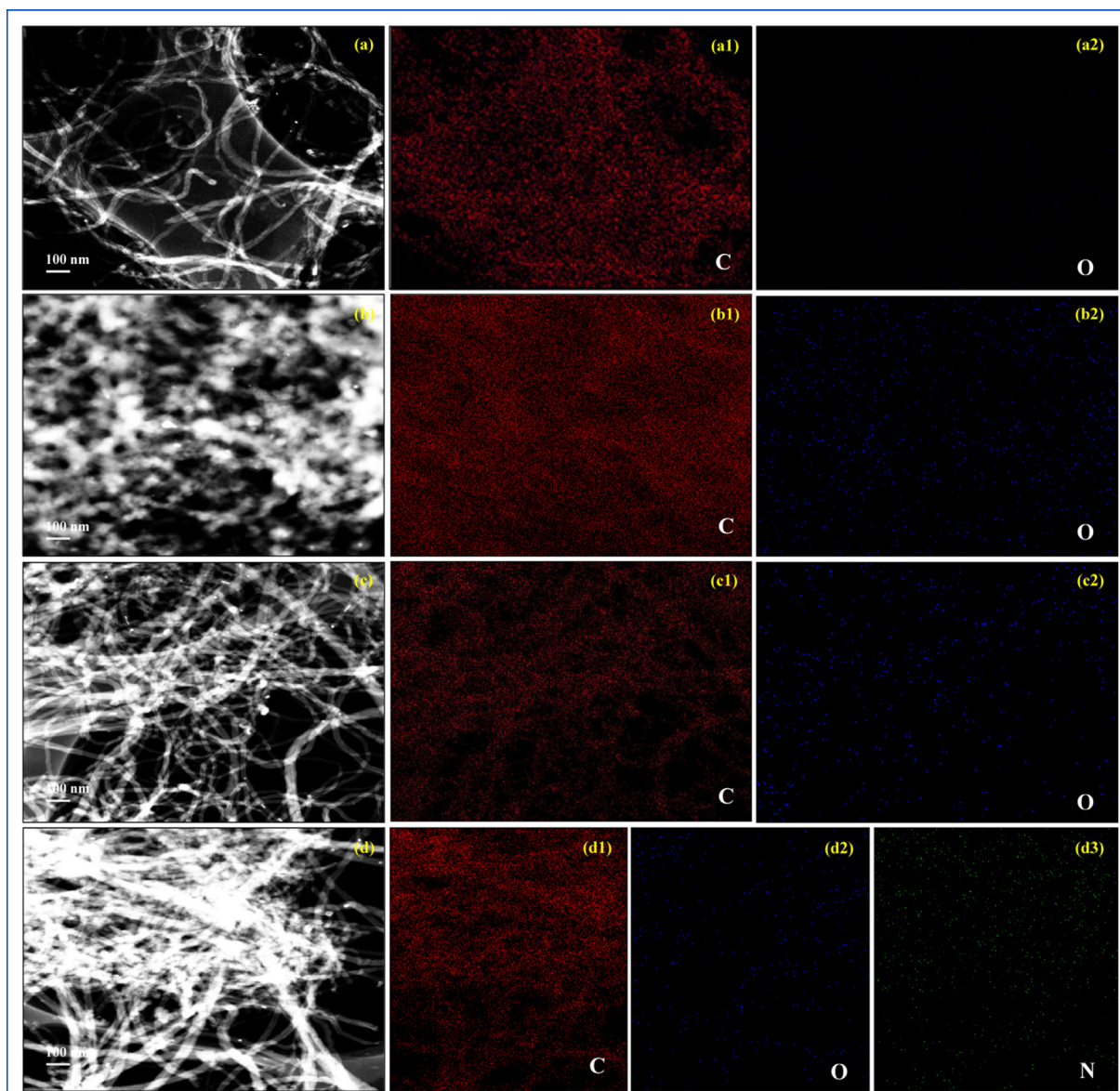
Fig. 11. HAADF-STEM images of MWCNTs (a), COOH-MWCNTs (b), OH-MWCNTs (c) and NH$_2$-MWCNTs (d) and their corresponding elemental mappings.

3.1.10. NH$_3$-TPD

The NH$_3$-TPD characterization in Fig. 13 provides the information of surface acidity of the samples. As can be seen in the TPD profiles, all the Ni based catalysts show two distinct NH$_3$ desorption peaks, indicating that there are a medium and a strong acidic sites, which is consistent with the reports of Gousi and Gao et al. [66]. Noticeably, compared with Ni/MWCNTs (Fig. 13(h)), oxygen-containing groups modified catalysts in Fig. 13(i) and (j) have higher intensity of NH$_3$ desorption peak, and the peak position shifts to higher temperature region, especially for Ni/COOH-MWCNTs. It because that introduction of oxygen-containing groups such as OH and COOH can obviously elevate the surface acidity of the catalysts [67]. Conversely, for Ni/NH$_2$-MWCNTs in Fig. 13(g), present relatively weak NH$_3$ desorption peak intensity, suggesting that the surface acidity decreases with the introduction of NH$_2$ group. Furthermore, it is worthwhile to note that all the N species modified catalysts exhibit drastically lower NH$_3$ desorption peak in comparison with Ni/MWCNTs, the strong acid peak in the range of 735–925 K and the medium acid peak in the range of

585–735 K shift to lower temperature region of 710–885 K and 540–725 K respectively. Therefore, incorporated N species into MWCNTs can result in more basicity sites on the supports, which can effectively neutralize the acidic sites on the surface of the catalyst. These results are confirmed by many researchers [28,68,69]. Typically, bifunctional N-Doped Co@C catalysts prepared by Long et al. showed that incorporation of N species into Co@NC could bring strong basic sites, which can effectively control the selectivity to primary amines as well as enhance nitriles transfer hydrogenation [68]. Li et al. used nitrogen-doped carbon supported iron catalysts in catalytic transfer hydrogenation of furfural and evidenced that Lewis-base sites can be formed by N doping so as to effectively promote the furfuryl alcohol selectivity [69]. Interestingly, as can be seen in Fig. 13(b)–(f), the acidity of the corresponding catalysts change obviously with the pyrolysis temperature, the higher the temperature, the stronger the desorption peak strength of NH$_3$, and it shifts to higher temperature region. The reason may be that the N content decreases with the increment of temperature so as to decrease the basicity.
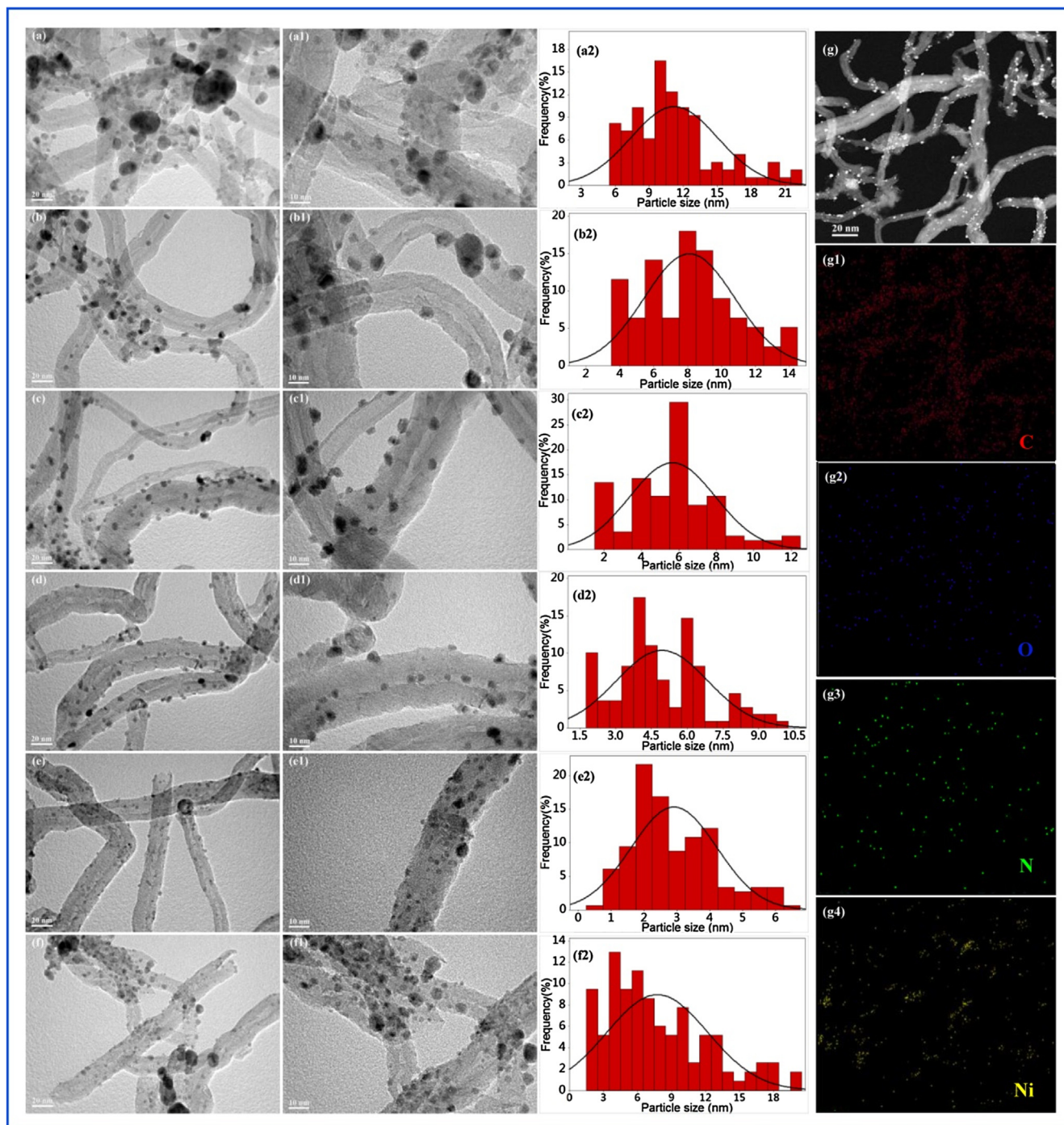
Fig. 12. TEM images of Ni/MWCNTs (a, a1), Ni/NH$_2$-MWCNTs (b, b1), Ni/COOH-MWCNTs (c, c1), Ni/OH-MWCNTs (d, d1), Ni/N-MWCNTs-800 (e, e1), Ni/N-MWCNTs-1000 (f, f1) and their corresponding histograms of NPs distribution (a2, b2, c2, d2, e2, f2) and HAADF-STEM image of Ni/N-MWCNTs-800 (g) and (g1, g2, g3, g4) the corresponding elemental mappings.

3.1.11. CO$_2$-TPD

CO$_2$-TPD was used to characterize the surface alkalinity of the samples. It can be observed from Fig. 14 that all the samples exhibits two CO$_2$ desorption peaks, the peak in the range of 385–485 K is ascribed to weak alkaline site, and the peak in the range of 575–700 K is attributed to strong alkaline site. There is almost no weak alkaline peak in Ni/COOH-MWCNTs (Fig. 14(a)) and Ni/OH-MWCNTs (Fig. 14(b)), it indicates that introduction of oxygen-containing group decreases the surface basicity [67]. However, Ni/NH$_2$-MWCNTs in Fig. 14(e) exhibits relatively stronger basic

desorption peak in comparison with Ni/MWCNTs. And it can be seen in Fig. 14(f)–(j) that the CO$_2$ desorption peaks become strong and shift to higher temperature region with the introduction of N species, further indicates that doping of N species can effectively increase the basicity [28,68,69]. In addition, it is interesting to note that the intensity of these two alkaline peaks decrease drastically and the position of the strong alkaline peak shifts to lower temperature when the pyrolysis temperature increases from 873 K to 1273 K, suggesting the decrement of the basicity. It because that the pyrolysis temperature has influence on nitrogen content and

Table 4
H_2 chemisorption data of Ni-based series catalysts.

Catalysts	H_2 uptake quantity ($\mu L\,g^{-1}$)	Metallic surface areas ($m^2\,g^{-1}$)	Dispersion (%)
Ni/MWCNT	68.57	0.57	2.57
Ni/NH$_2$-MWCNTs	94.63	0.68	4.61
Ni/COOH-MWCNTs	107.41	0.71	5.87
Ni/OH-MWCNTs	119.69	0.74	6.41
Ni/N-MWCNTs-600	111.73	0.72	5.96
Ni/N-MWCNTs-700	132.58	0.79	8.34
Ni/N-MWCNTs-800	139.32	0.83	8.56
Ni/N-MWCNTs-900	124.37	0.77	7.62
Ni/N-MWCNTs-1000	92.63	0.67	4.53
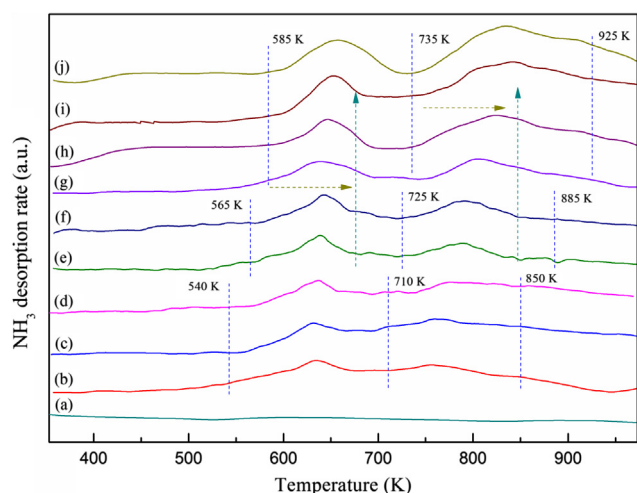
Fig. 13. NH$_3$-TPD profiles of MWCNTs (a), Ni/N-MWCNTs-600 (b), Ni/N-MWCNTs-700 (c), Ni/N-MWCNTs-800 (d), Ni/N-MWCNTs-900 (e), Ni/N-MWCNTs-1000 (f), Ni/NH$_2$-MWCNTs (g), Ni/MWCNTs (h), Ni/OH-MWCNTs (i) and Ni/COOH-MWCNTs (j).

Fig. 14. CO$_2$-TPD profiles of Ni/COOH-MWCNTs (a), Ni/OH-MWCNTs (b), Ni/MWCNTs (c), MWCNTs (d), Ni/NH$_2$-MWCNTs (e), Ni/N-MWCNTs-600 (f), Ni/N-MWCNTs-700 (g), Ni/N-MWCNTs-800 (h), Ni/N-MWCNTs-900 (i) and Ni/N-MWCNTs-1000 (j).

nitrogen species type, so as to affect the alkalinity of the samples. The results are well in accordance with NH$_3$-TPD characterization in Fig. 13.

3.2. Catalytic performance

The catalytic performances over different catalysts are illustrated in Fig. 15. ADN hydrogenation is a complicated process (Path 1) with different reaction pathways and many intermediates such as cyclic or chain amines and diamines, ACN and HDA are the desired products accompanied with the by-products of ACH, dimers and C$_{12}$ amines. Therefore, it is always a challenge for ADN hydrogenation to obtain high selectivity to primary amines of ACN and HDA at high ADN conversion. Since the formation of N-substituted imines requires deamination, it has to inhibit the formation of by-products by adding a large amount of ammonia and alkali metal hydroxides [2,5–7,9,10,19]. Similarly, the intermediates of imines and amines formed during ADN hydrogenation are favorable to condensation and deamination over the acidic sites of the catalysts, thus reducing the selectivity to primary amines. Therefore, increasing the alkalinity of the catalyst by introduction of basic oxide or using alkaline support is helpful to produce primary amines [3–5,8,11,12,14,16–18,20–22]. It is important to obtain higher selectivity with higher ADN conversion under moderate reaction conditions. It has been found that modifying the surface of CNTs with functional group species or N species can effectively prevent the aggregation of metal nanoparticles so as to obtain ultrasmall metal particle size and better dispersion, and
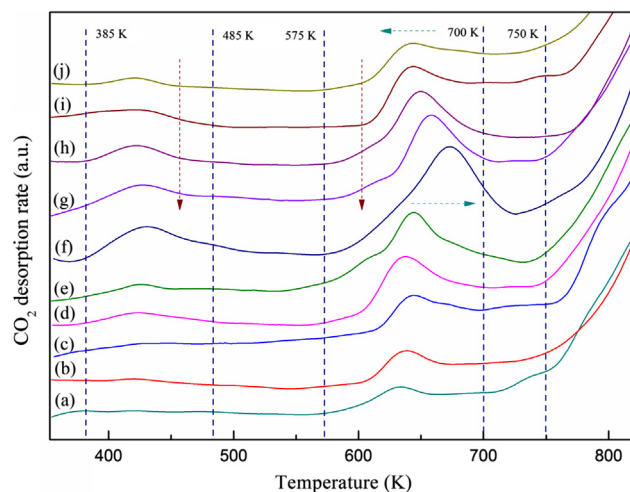
thus promote catalytic hydrogenation activities [27–33]. Chen et al. found that the interaction between cobalt nanoparticles and oxygen- and nitrogen functionalized carbon nanotubes will obviously boost catalytic nitrobenzene hydrogenation due to ultra-dispersed cobalt nanoparticles and higher cobalt reducibility [31]. Moreover, Shi et al. also found that ultrasmall-sized Pt nanoparticles (~1 nm) formed in nitrogen and oxygen functional groups modified MWCNTs and showed superior catalytic performances in nitroarenes hydrogenation [33]. Importantly, it has shown that incorporated N species could bring strong basic sites, which can act as the role similar to the addition of bases [28,68,69]. Therefore, different functional groups such as NH$_2$—, COOH—, OH— and N species functionalized MWCNTs supported Ni catalysts were prepared and applied in ADN hydrogenation under different temperature of 318–348 K, and the results are presented in Fig. 15. It can be observed from Fig. 15 that functional group and N species functionalized MWCNTs supported Ni catalysts possess different catalytic performance under the same reaction conditions, suggesting that the functional group and N species can effectively act on Ni nanoparticles and adjust the acidity and basicity. In detail, as seen in Fig. 15(A), (C) and (E), the functional group such as NH$_2$—, COOH— and OH— modified MWCNTs supported Ni catalysts present higher ADN conversion in comparison with Ni/MWCNTs. The above characterization results show that —NH$_2$, —COOH, —OH on the surface of MWCNTs can effectively act on metal ions by electrostatic attractions and chemical interactions to provide nucleation sites, thus promote the Ni nanoparticles dispersion, and hence improve the catalytic hydrogenation activity. Moreover, XRD in Fig. 2, H$_2$-TPR in Fig. 4, XPS in Fig. 10, and TEM in Fig. 12 also have confirmed that higher dispersion and smaller of Ni nanoparticles, lower reduction activation energy of NiO, larger amounts of Ni^{0+} are presented on functional group modified MWCNTs supported catalysts. Furthermore, H$_2$ chemisorption data in Table 4 show higher H$_2$ uptake quantity, metallic surface areas and metallic dispersion than Ni/MWCNT, which is in accordance with the result of high catalytic hydrogenation activity. Moreover, it can be observed from Fig. 15(c) and (d) that Ni/COOH-MWCNTs and Ni/OH-MWCNTs present lower selectivity to primary amines at almost the same ADN conversion as compared to Ni/MWCNTs. Ni/MWCNTs gives 93.19% ADN conversion and 81.92% selectivity to primary amines of ACN and HDA under 338 K, however, Ni/COOH-MWCNTs presents lower primary amines selectivity of 76.44% at ADN conversion of 91.84% under
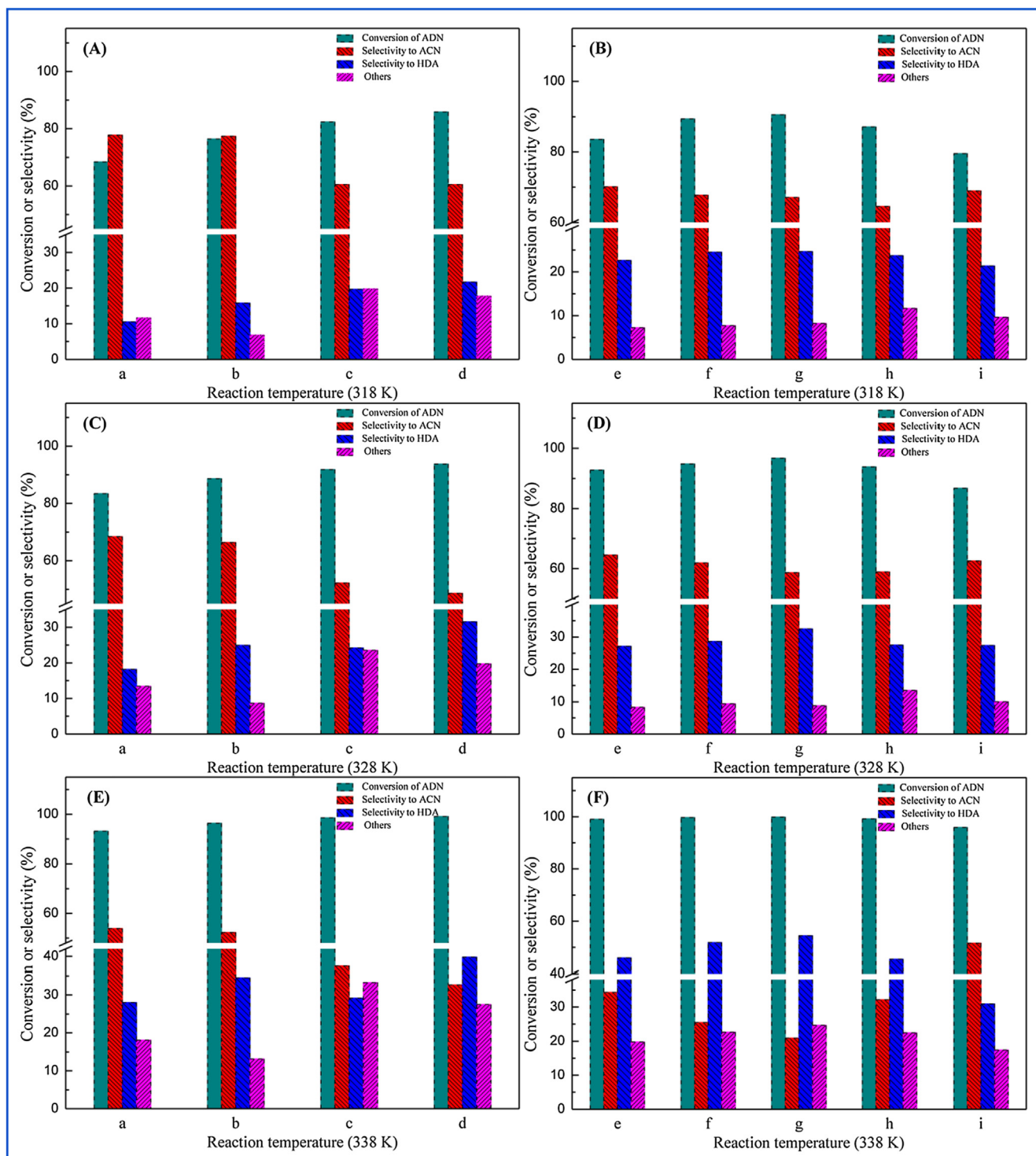
Fig. 15. Catalytic performance of Ni/MWCNTs (a), Ni/NH$_2$-MWCNTs (b), Ni/COOH-MWCNTs (c), Ni/OH-MWCNTs (d), Ni/N-MWCNTs-600 (e), Ni/N-MWCNTs-700 (f), Ni/N-MWCNTs-800 (g), Ni/N-MWCNTs-900 (h) and Ni/N-MWCNTs-1000 (i) under different reaction temperature; Reaction conditions: Stirring rate, 750 rpm; P_{H2}, 2.0 MPa; Time, 6 h; Ni loading, 20 wt%; Reduction temperature, 623 K; Ethanol, 15 mL; ADN, 1.0 g; Catalyst, 0.21 g. Others: mainly including 1-azacycloheptane (ACH).

328 K. The characterization results of NH$_3$-TPD (Fig. 13) and CO$_2$-TPD (Fig. 14) show that introduction of oxygen-containing groups into MWCNTs can obviously increase the acidity of the catalyst, which is in favor of the formation of by-products. Conversely, in comparison with 83.43% ADN conversion and 86.55% selectivity to primary amines over Ni/MWCNTs, Ni/NH$_2$-MWCNTs in Fig. 15 (b) gives higher conversion of 88.63% and higher selectivity of 91.34%, indicating that introduction of NH$_2$ group to MWCNTs

can effectively increase the basicity which is in favor of the primary amines production.

Significantly, the catalytic performances of N species modified MWCNTs supported catalysts under different reaction temperature are illustrated in Fig. 15(B), (D) and (F) and show higher ADN conversion and selectivity to primary amines as compared to Ni/MWCNTs under the same reaction conditions. The conversion and selectivity to primary amines of ACN and HDA over

Ni/N-MWCNTs-800 increase 13.29% and 4.66% under 328 K. The results confirm that incorporated N species into MWCNTs can effectively act on NiO by strong electronic interactions so as to form ultra-small particles, hence promote NiO reduction and Ni nanoparticles dispersion, thereby drastically enhance the catalytic hydrogenation activity [27,28,31–33]. And the characterizations such as XRD in Fig. 2, Raman spectra in Fig. 3, H_2-TPR in Fig. 4, XPS in Fig. 10, and TEM in Fig. 12 also confirm this. What's more, many researchers have proved that introduction of N can act as similar as the role of addition of base and improve the surface alkalinity of the catalyst, thus improve the selectivity to primary amines of ACN and HDA, and the improvement of surface alkalinity was testified by NH_3-TPD and CO_2-TPD in Figs. 13 and 14 [28,68,69]. Typically, Long et al synthetized bifunctional N-Doped Co@C and applied in nitriles transfer hydrogenation, it was found that the incorporation of N species into Co@NC could bring strong basic sites which effectively improve the selectivity to primary amines as well as enhance hydrogenation activity [68]. Interestingly, the pyrolysis temperature can effectively influence the N content and N species type, so as to affect the interaction between N species and Ni nanoparticles and then has influence on the catalytic hydrogenation activity. Ni/N-MWCNTs-800 possesses the highest ADN conversion of 96.72% under 328 K. It has been reported that pyridinic N can serve as main metal-binding sites for transition-metal species [58,60] and main active sites for promoting the reduction of metallic oxide [27,28,57]. XPS results in Fig. 9 show that N-MWCNTs-800 possesses the highest content ratio of pyridinic N. Meanwhile, XRD in Fig. 2, Raman spectra in Fig. 3, H_2-TPR in Fig. 4, XPS in Fig. 10, and TEM in Fig. 12 indicate that Ni/N-MWCNTs-800 present the most defect sites, the smallest Ni nanoparticles and the highest dispersion, the lowest NiO reduction activation energy, and the highest content of Ni^{0+}. Furthermore, Ni/N-MWCNTs-800 (Table 4) possesses the highest H_2 uptake quantity, metallic surface areas and dispersion. Therefore, Ni/N-MWCNTs-800 gives the best catalytic performance of 96.72% ADN conversion and 91.21% selectivity to primary amines of ACN and HDA.

Noticeably, according to the results in Fig. 15, the selectivity to by-products is still about 10% at 95% conversion even after optimization of the reaction conditions. Moreover, higher temperature leads to higher ADN conversion and a large number of by-products mainly including 1-azacycloheptane (ACH). It can be seen from Fig. 15 that the selectivity to by-products increase drastically to 24.67% when the ADN conversion reaches to 99.87% over Ni/N-MWCNTs-800 under 338 K. Here, we used small amount of basic ionic liquids 1-butyl-3-methylimidazolium hydroxide ([Bmim]OH) as a switch for adjusting the selectivity to primary amines of ACN and HDA. The effects of different amount of [Bmim]OH ethanol solution (25%) on the selectivity to ACN and HDA in ADN hydrogenation over Ni/N-MWCNTs-800 are illustrated in Fig. 16. The selectivity to primary amines increases significantly with the increment of [Bmim]OH under almost the same ADN conversion, indicating that [Bmim]OH can effectively inhibit the formation of by-products. Typically, the selectivity to primary amines of ACN and HDA is up to 97.80% at 95.34% ADN conversion with the addition of 0.15 g [Bmim]OH ethanol solution (25%). Fig. 17 presents the catalytic performance over different catalysts under [Bmim]OH ethanol solution (25%) system. It can be observed from Fig. 17 that the selectivity to primary amines of ACN and HDA is up to 97% in [Bmim]OH system. The reason how [Bmim]OH inhibits the formation of by-products may be attributed to two factors, one is that OH— ions in basic [Bmim]OH can effectively suppress the acidic sites on catalyst surface so as to inhibit condensation and deamination process on acidic sites, the other is that [Bmim]OH can effectively stabilize the —NH_2 groups in the amino-imine intermediates so as to inhibit nucleophilic addition of the primary
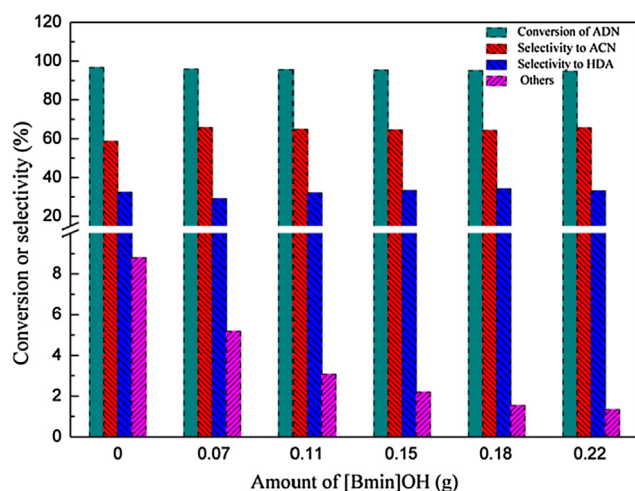

Fig. 16. The effects of different amount of [Bmim]OH ethanol solution (25%) on the controllability of ACN and HDA selectivity for the hydrogenation of ADN over Ni/N-MWCNTs-800; Reaction conditions: Stirring rate, 750 rpm; P_{H2}, 2.0 MPa; Time, 6 h; Ni loading, 20 wt%; Ethanol, 15 mL; ADN, 1.0 g; Catalyst, 0.21 g. Others: mainly including 1-azacycloheptane (ACH).
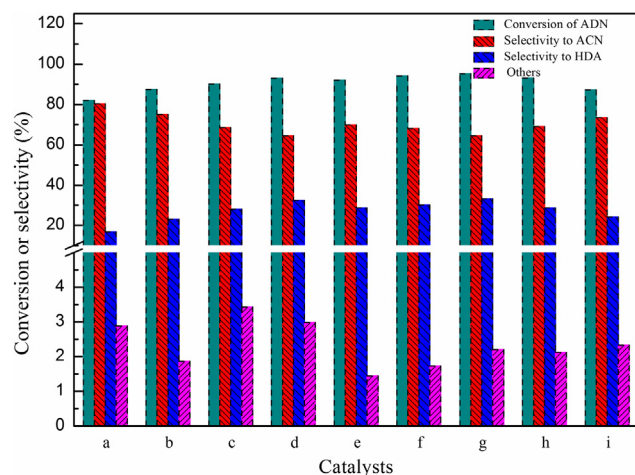

Fig. 17. Catalytic performance of Ni/MWCNTs (a), Ni/NH$_2$-MWCNTs (b), Ni/COOH-MWCNTs (c), Ni/OH-MWCNTs (d), Ni/N-MWCNTs-600 (e), Ni/N-MWCNTs-700 (f), Ni/N-MWCNTs-800 (g), Ni/N-MWCNTs-900 (h) and Ni/N-MWCNTs-1000 (i) under [Bmim]OH ethanol solution (25%) system. Reaction conditions: Stirring rate, 750 rpm; Reaction temperature 328 K; P_{H2}, 2.0 MPa; Time, 6 h; Ni loading, 20 wt %; Reduction temperature, 623 K; [Bmim]OH ethanol solution (25%), 0.15 g; Ethanol, 15 mL; ADN, 1.0 g; Catalyst, 0.21 g. Others: mainly including 1-azacycloheptane (ACH).

amine to α-carbon of aldimine and then impede by-products formation.

Additionally, plausible mechanism for the hydrogenation of ACN to HDA and ACH in the presence of [Bmim]OH are illustrated in Path 2. The optimized structures of intermediates and transition states with bond distance (in Å) for ACN hydrogenation in the presence of [Bmim]OH are depicted in Fig. 18, and the potential comparative free energy of IM1 to IM3 along Path 1 and ACN hydrogenation in the presence of [Bmim]OH along Path 2 are shown in Fig. 19. As seen in Fig. 18, firstly, [Bmim]OH can combine with ACN to form a macromolecular complex 1 by hydrogen bonding, which is more steady structure in comparison with reactants by 11.3 Kcal/mol (Fig. 19). Subsequently, the OH— ions of the basic [Bmim]OH can activate ACN by depriving of the H proton from the —NH_2 group to from complex 2 via transition state TS (1/2). In TS (1/2), the newly formed N1—H2 bond and O1—H1 bond are
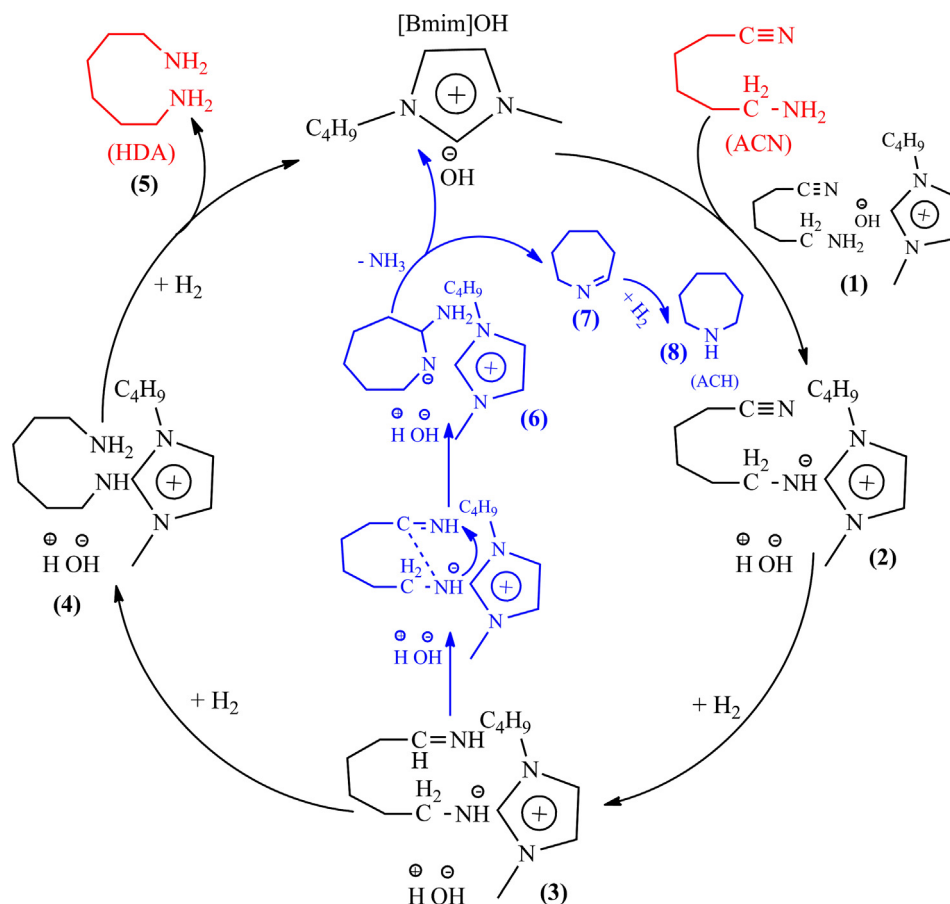
Path 2. plausible mechanism for the hydrogenation of ACN to HDA and ACH in the presence of [Bmim]OH.

shortened to 1.031 Å and 0.989 Å, and the two broken N1—H1 and O1—H2 bonds are elongated to 2.176 Å and 2.847 Å, indicating that ACN is activated by breaking the N1—H1 and form a highly electronegativity N1 atom [36,37]. The following step is hydrogenation of —C≡N group of complex 2 to form imines complex 3 via TS (2/3). Subsequently, complex 3 can further hydrogenated to amines complex 4 via TS (3/4), followed by [Bmim]OH regeneration via TS (4/5). In TS (4/5), the N1—H1 bond is shortened from 1.800 Å to 1.037 Å and the N1—H2 and O1—H1 bonds are elongated to 3.493 Å and 2.029 Å, suggesting that the H1 proton is migrated from H₂O to —N1H3 stabilized by [Bmim]OH and finally leads to the product of HDA. Significantly, it can be seen from Path 2 that the active intermediate imines (—CH=NH) of complex 3 need capture the single H proton of —NH stabilized by [Bmim]OH to form complex 6 via TS (3/6), then it can be deaminated by depriving of the H proton of H₂O to form complex 7 via TS (6/7), and then it can be hydrogenated to ACH by TS (7/8). In TS (3/6), the two N2—H3 and C1—N1 bonds are formed and the N1—H3 bond is broken, however, the distances of N2—H3 and C1—N1 are up to 2.369 Å and 2.493 Å, and the distance of N1—H3 is 1.021 Å, which is shorter than N1—H3 in complex 3. Moreover, the energy barrier from complex 3 to TS (3/6) is up to 35.6 Kcal/mol (Fig. 19), indicating that this process is difficult to happen because it is hard for imines to abstract a H proton from —NH stabilized by [Bmim]OH to take place intramolecular condensation. Furthermore, in TS (6/7), the C1—N1 (1.280 Å) double bond is formed since C1—N1 (1.472 Å) bond is shortened and the C1—N2 (2.618 Å) and O1—H1 (0.983 Å) are broken by migrating H1 from H₂O to N2 atom. The energy barrier from complex 6 to TS (6/7) is up to 59.8 Kcal/mol, suggesting that the H migration and deamination

process is difficult. Noteworthy, as can be seen in Fig. 19(a) that the energy barriers from IM1 to TS (IM1/IM2) and IM2 to TS (IM2/IM3) (seeing Path 1) are only 19.5 Kcal/mol and 20.6 Kcal/-mol, which are smaller than the above cyclization and deamination process in the presence of [Bmim]OH. Consequently, the process in Path 2 are clearly shown that [Bmim]OH can effectively stabilize the —NH₂ group of ACN, and thus decreases the nucleophilicity of the primary amine as well as slows down the nucleophilic attack on the intermediate imine so as to almost completely inhibit nucleophilic addition of the primary amine to the α-carbon of aldimine, hence impedes the secondary amine production (mainly 1-azacycloheptane (ACH)). Therefore, this may be the plausible mechanism for obtaining high selectivity to ACN and HDA in the presence of [Bmim]OH. Similarly, Ren and Patil have confirmed that [Bmim]OH can effectively stabilize the —NH₂ of 2-aminobenzonitriles, and thus favor CO₂ nucleophilic addition to form quinazoline-2,4(1H,3H)-diones, and a comprehensive and detailed reaction mechanism was proposed by Ren via density functional theory calculations [36,37].

Fig. 20 illustrates the effects of reaction conditions on the catalytic performance over Ni/N-MWCNTs-800 in [Bmim]OH system. It can be seen from the results in Fig. 20 (a) that ADN conversion increases with the increment of reaction temperature, and it is higher than 98% when the reaction temperature reaches to 338 K. However, the selectivity to ACN decreases sharply when the reaction temperature increases from 318 K to 348 K, and the selectivity to HDA increases drastically as well as the selectivity to by-products increases gradually. Therefore, higher temperature results in deep hydrogenation, and thus produces HDA and much more by-products. HDA is mainly formed under relatively high
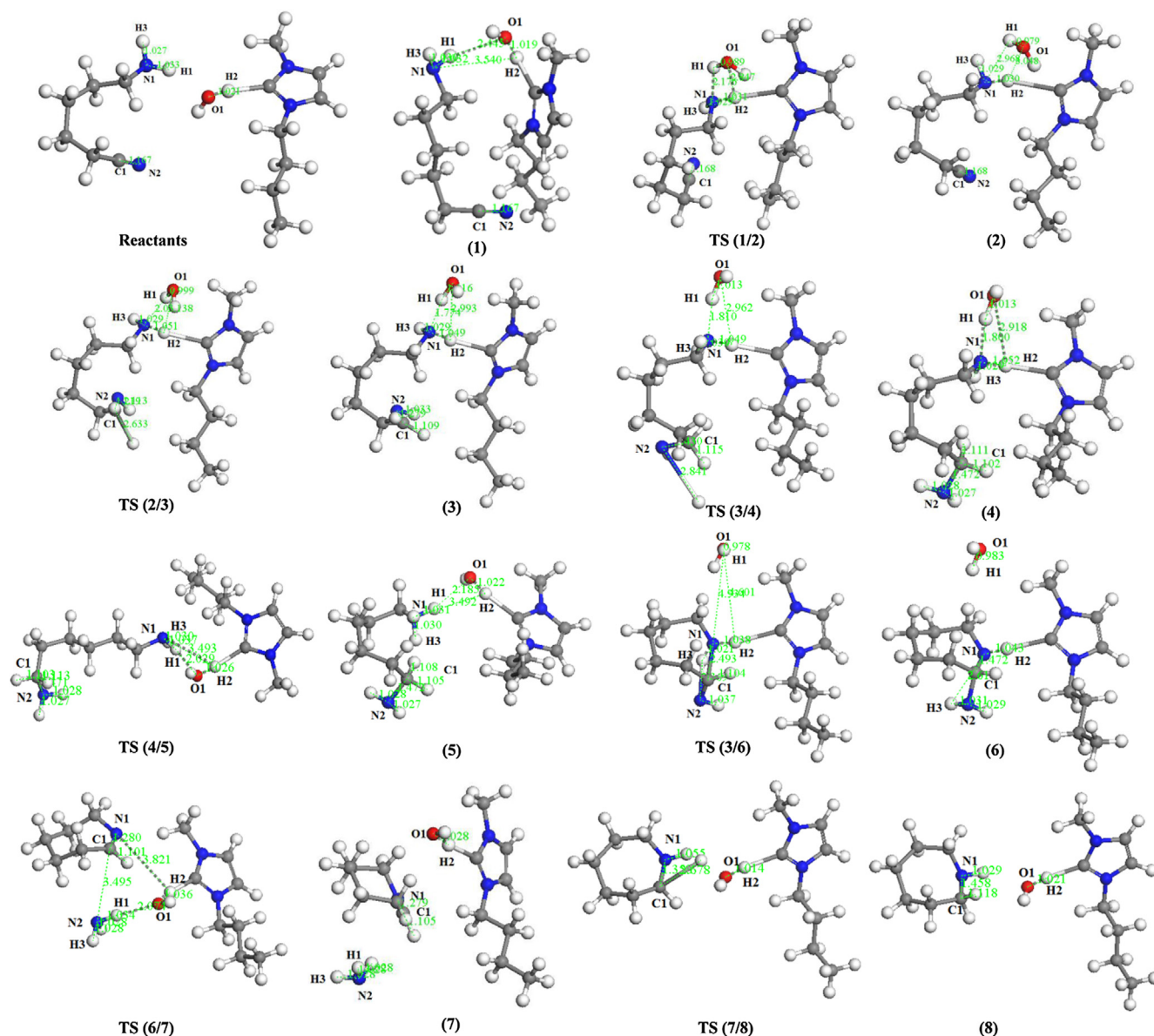
Fig. 18. Optimized structures with bond distance (in Å) for ACN hydrogenation in the presence of [Bmim]OH.

temperature and due to the stabilization of —NH$_2$ in ACN by [Bmim]OH, the selectivity to ACN is only 4.83% and the selectivity to HDA is up to 90.39% under 348 K when ADN conversion reaches to 100%. However, when the reaction temperature increases to 358 K, the products mainly include HDA and by-products, and the selectivity to by-products is up to 10.77% since high temperature can break the stabilization of —NH$_2$ in ACN by [Bmim]OH in a certain degree. Fig. 20(b) illustrates the effect of H$_2$ pressure under 328 K. ADN conversion increases gradually with the increment of pressure. In addition, the effect of H$_2$ pressure on the selectivity to ACN, HDA and by-products are similar to that of temperature. Typically, when the H$_2$ pressure is 0.5 MPa, the selectivity to ACN is maintained at 81.82% and the selectivity to HDA is 16.74% with the 90.16% conversion of ADN, suggesting that [Bmim]OH can inhibit deep hydrogenation of the partial hydrogenation product of ACN to HDA and by-products at relatively low H$_2$ pressure. Furthermore, the effects of reaction time and the amounts of Ni loading can be observed in Fig. 20(c) and (d). Similarly, ADN conversion increases obviously with the increment of reaction time and Ni loading amounts, and the effects on the selectivity to ACN, HDA

and by-products are similar to that of H$_2$ pressure in Fig. 20(a) and (b). In a word, it gives 97.80% total selectivity to ACN and HDA at 95.34% ADN conversion over Ni/N-MWCNTs-800 in [Bmim]OH system under optimized reaction conditions.

3.3. The recycle of the catalysts

The reusability of Ni/N-MWCNTs-800 is shown in Fig. 21. The catalyst is recycled after centrifugal separation, ethanol washing and vacuum drying at 353 K for 8 h. As can be seen in Fig. 21 that the changes of ADN conversion and products selectivity are not obvious for five run times, ADN conversion is more than 90% and the selectivity to primary amines are almost unchanged for the fifth recycle. Noticeably, Fig. 22 presents the TEM images and Ni 2p$_{3/2}$ XPS patterns of fresh and fifth run of Ni/N-MWCNTs-800. As seen in Fig. 22(a) and (c), the tendency of Ni nanoparticles aggregation on Ni/N-MWCNTs-800 is not particularly significant, the reason may be that the N species can effectively favor the dispersion so as to prevent the aggregation of Ni nanoparticles. Moreover, the Ni 2p$_{3/2}$ XPS patterns in Fig. 22(b) and (d) show that fifth run of
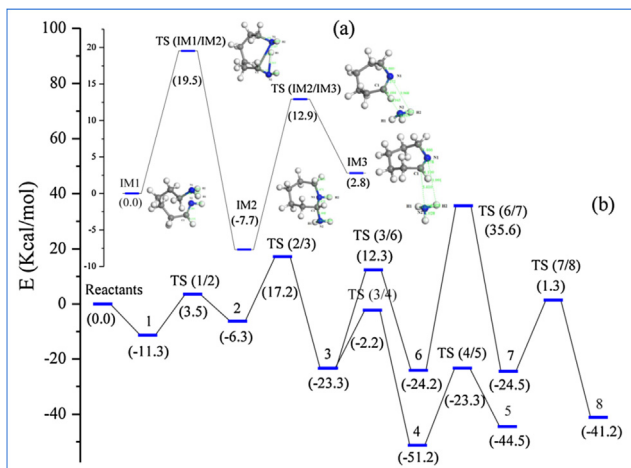
Fig. 19. Calculated energy profiles for potential comparative free energy of IM1 to IM3 along Path 1(a) and ADN hydrogenation in the presence of [Bmim]OH along Path 2(b).
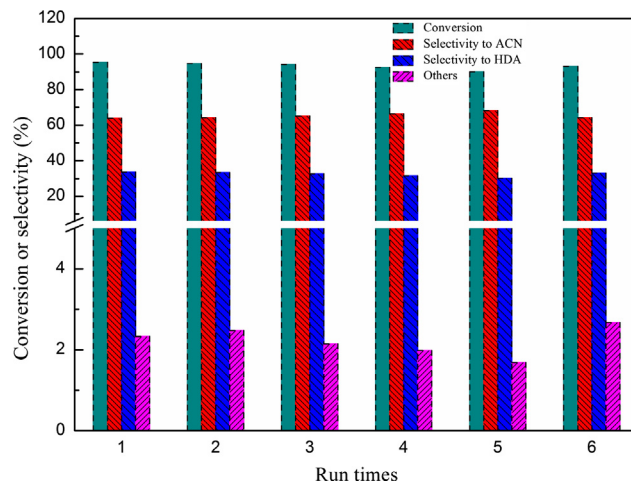

Fig. 21. Reusability of Ni/N-MWCNTs-800; Reaction conditions: Stirring rate, 750 rpm; Reaction temperature 328 K; P_{H2}, 2.0 MPa; Time, 6 h; Ni loading, 20 wt %; Ethanol, 15 mL; [Bmim]OH ethanol solution (25%), 0.15 g; ADN, 1.0 g; Catalyst, 0.21 g; Others: mainly including 1-azacycloheptane (ACH). 6 run times: the five recycle of the Ni/N-MWCNTs-800 was re-activated in hydrogen fluid at 623 K for 4 h.

Ni/N-MWCNTs-800 has 31.21% peak area ratio of Ni^{0+} as compared with 39.33% peak area ratio of Ni^{0+} in fresh catalyst. Furthermore, Ni/N-MWCNTs-800 used for fifth run times was re-activated in hydrogen fluid at 623 K for 4 h and applied in sixth recycle, and the results show that the ADN conversion reaches to 93.12% and

the selectivity to ACN and HDA is 97.33%. Similarly, some researchers also found that incorporated N species can effectively inhibit the metal nanoparticles aggregation and reoxidation [31,33,63].
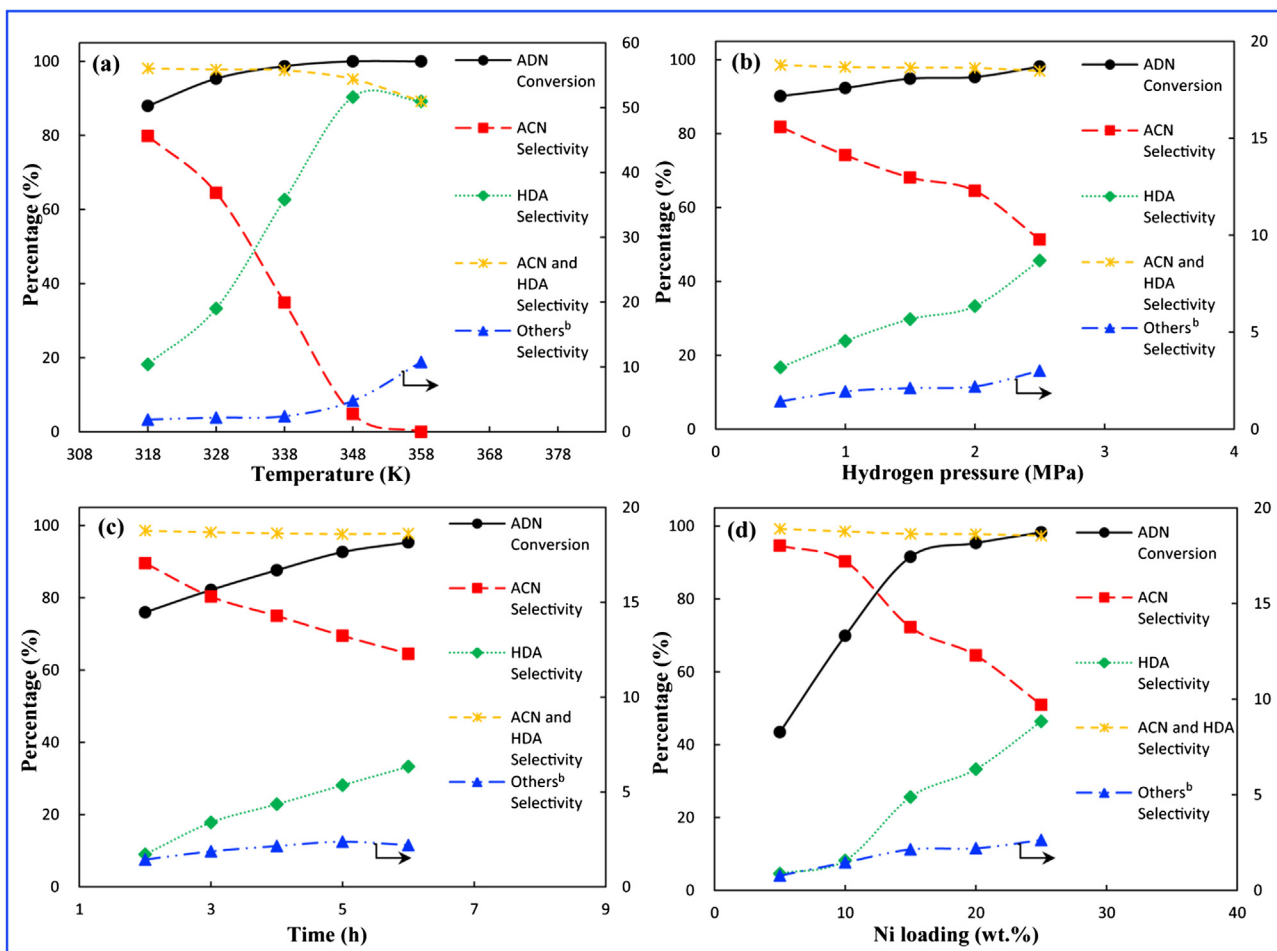

Fig. 20. Effects of reaction conditions over Ni/N-MWCNTs-800 reaction temperature (a), hydrogen pressure (b), reaction time (c) and amounts of Ni loading (d) (Different reaction conditions: (a) P_{H2}, 2.0 MPa; Time, 6 h; Ni loading, 20 wt%; (b) Reaction temperature 328 K; Time, 6 h; Ni loading, 20 wt%; (c) Reaction temperature 328 K; P_{H2}, 2.0 MPa; Ni loading, 20 wt%; (d) Reaction temperature 328 K; P_{H2}, 2.0 MPa; Time, 6 h. Identical reaction conditions: Stirring rate, 750 rpm; Reduction temperature, 623 K; [Bmim]OH ethanol solution (25%), 0.15 g; Ethanol, 15 mL; ADN, 1.0 g; Catalyst, 0.21 g;. [b]Others: mainly including 1-azacycloheptane (ACH).
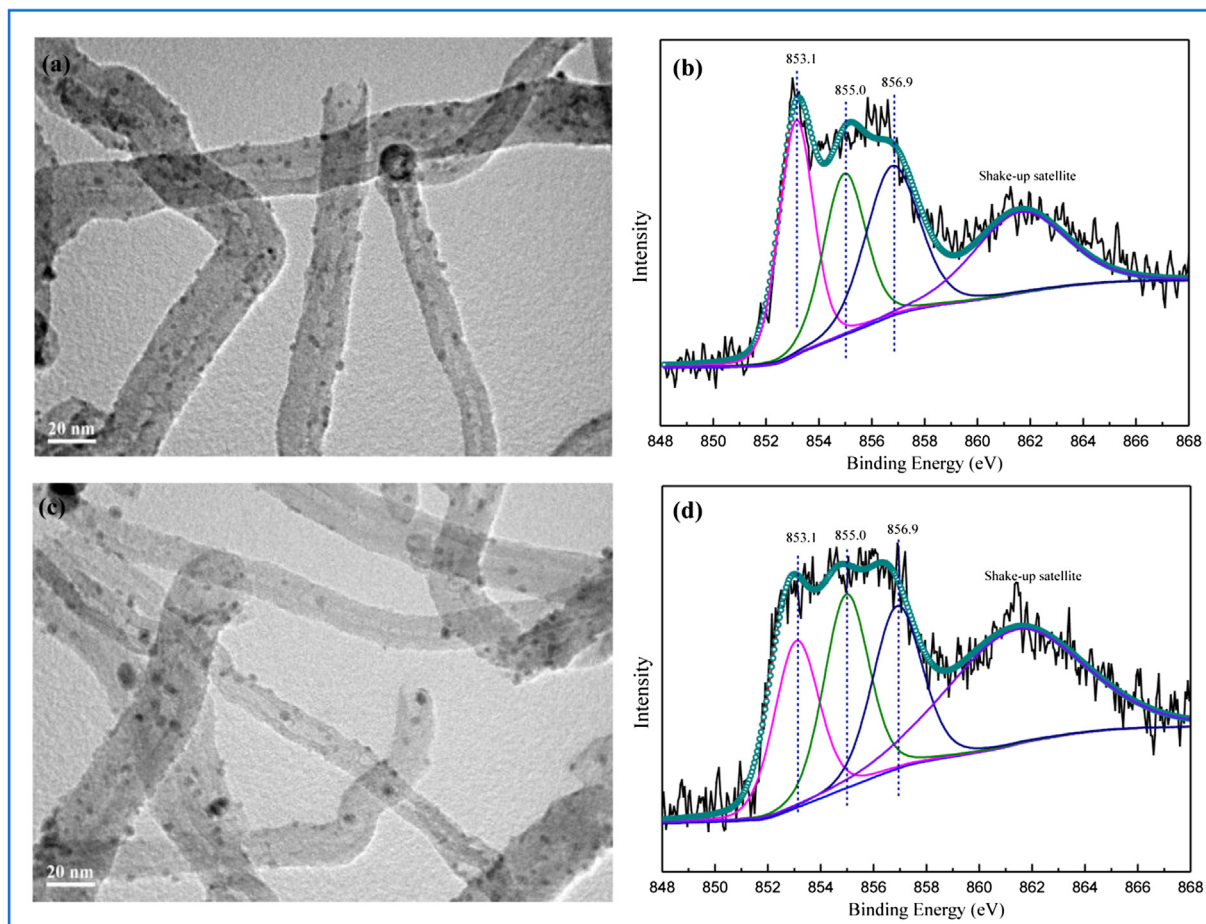
Fig. 22. TEM images of fresh Ni/N-MWCNTs-800 (a) and fifth run of Ni/N-MWCNTs-800 (c); Ni 2p$_{3/2}$ XPS patterns of fresh Ni/N-MWCNTs-800 (b) and fifth run of Ni/N-MWCNTs-800 (d).

4. Conclusions

Amine-, carboxyl-, hydroxyl- and nitrogen modified multi-walled carbon nanotubes (NH$_2$-MWCNTs, COOH-MWCNTs, OH-MWCNTs and N-MWCNTs-T) supported nickel-based catalysts were prepared by wetness impregnation-reduction method and applied in ADN hydrogenation to ACN and HDA. It was found that different functional groups such as NH$_2$—, COOH—, OH— on the surface of MWCNTs can effectively act on metal ions by electrostatic attractions and chemical interactions so as to provide nucleation sites, and N species in MWCNTs can act as active sites for the Ni deposition due to the strong electronic interactions between N species and Ni so as to promote ultra-small Ni nanoparticles formation, decrease the reduction activation energy of NiO, increase the amounts of zero-valent Ni as well as the Ni nanoparticles dispersion. Furthermore, the doped N on MWCNTs increases the lewis basicity, which favors the formation of primary amine of ACN and HDA. Moreover, the basic ionic liquid [Bmim]OH may switch the selectivity by inhibiting nucleophilic addition of the primary amine to the α-carbon of aldimine *via* the stabilization of —NH$_2$ groups in the amino-imine intermediates so as to impede by-products formation. In addition, the mechanism for ADN hydrogenation in [Bmim]OH was studied by density functional theory calculations. Under optimized conditions, the selectivity to ACN is up to 81.82% at the ADN conversion of 90.16% or the selectivity to HDA is up to 90.39% at the 100% ADN conversion, especially it gives 97.80% total selectivity to ACN and HDA at 95.34% conversion of ADN over Ni/ N-MWCNTs-800 in the presence of [Bmim]OH.

References

[1] Y. Saito, H. Ishitani, M. Ueno, S. Kobayashi, Chem. Open 6 (2) (2017) 211.
[2] V. Balladur, P. Fouilloux, C. Bellefon, Appl. Catal. A 133 (2) (1995) 367.
[3] M. Serra, J. Catal. 209 (2002) 202.
[4] M. Serra, P. Salagre, Y. Cesteros, F. Medina, J.E. Sueiras, Appl. Catal. A 272 (2004) 353.
[5] D. Tichit, R. Durand, A. Rolland, B. Coq, J. Lopez, P. Marion, J. Catal. 211 (2002) 511.
[6] M.C. Cotting, L. Gilbert, US Patent 5,981,790 (1999), to Rhone-Poulenc Fiber and Resin Intermediates.
[7] M. Harper, WO Patent 00,27526A1 (2000), to E.I. Du Pont de Nemours and Company.
[8] H. Li, Y. Xu, H. Li, J.F. Deng, Appl. Catal. A 216 (1) (2001) 51.
[9] H. Li, Y. Xu, J.F. Deng, New J. Chem. 23 (11) (1999) 1059.
[10] X. Yu, H. Li, J.F. Deng, Appl. Catal. A 199 (2) (2000) 191.
[11] F. Medina, P. Salagre, J.E. Sueiras, J.L.G. Fierro, Solid State Ionics 59 (1993) 205.
[12] F. Medina, P. Salagre, J.E. Sueiras, J.L.G. Fierro, J. Mol. Catal. 81 (1993) 387.

[13] F. Medina, P. Salagre, J.E. Sueiras, J.L.G. Fierro, J. Chem. Soc. Faraday Trans. 89 (1993) 3507.
[14] F. Medina, P. Salagre, J.E. Sueiras, J.L.G. Fierro, Appl. Catal. A 99 (2) (1993) 115.
[15] F. Medina, P. Salagre, J.E. Sueiras, J.L.G. Fierro, J. Chem. Soc. Faraday Trans. 90 (10) (1994) 1455.
[16] Y. Lv, F. Hao, S. Xiong, P. Liu, H.A. Luo, RSC Adv. 6 (65) (2016) 60933.
[17] Y. Lv, F. Hao, P. Liu, S. Xiong, H.A. Luo, J. Mol. Catal. A: Chem. 426 (2017) 15.
[18] Y. Lv, F. Hao, P. Liu, S. Xiong, H. Luo, React. Kinet. Mech. Catal. 119 (2) (2016) 555.
[19] Z. Jia, B. Zhen, M. Han, C. Wang, Catal. Commun. 73 (2016) 80.
[20] H. Liao, S. Liu, F. Hao, P. Liu, K. You, D. Liu, H.A. Luo, React. Kinet. Mech. Catal. 109 (2) (2013) 475.
[21] S. Liu, F. Hao, P. Liu, H. Liao, Res. Chem. Intermed. 41 (8) (2015) 5879.
[22] Y. Lv, J. Li, S. Feng, P. Liu, F. Hao, W. Xiong, H. Luo, Chem. Eng. J. 346 (2018) 203.
[23] S. Alini, A. Bottino, G. Capannelli, A. Comite, S. Paganelli, Appl. Catal. A 292 (2005) 105.
[24] S. Alini, A. Bottino, G. Capannelli, R. Carbone, A. Comite, G. Vitulli, J. Mol. Catal. A: Chem. 206 (1) (2003) 363.
[25] Z. Ma, H. Zhang, Z. Yang, G. Ji, B. Yu, X. Liu, Z. Liu, Green Chem. 18 (7) (2016) 1976.
[26] Y. Yan, J. Miao, Z. Yang, F. Xiao, H.B. Yang, B. Liu, Y. Yang, Chem. Soc. Rev. 44 (10) (2015) 3295.
[27] R. Nie, H. Jiang, X. Lu, D. Zhou, Q. Xia, Catal. Sci. Technol. 6 (2016) 1913.
[28] Y. Suna, L. Chen, Y. Bao, G. Wang, Y. Zhang, M. Fu, J. Wu, D. Ye, Catal. Today 307 (2018) 212.
[29] M. Davari, S. Karimi, A. Tavasoli, A. Karimi, Appl. Catal. A 485 (2014) 133.
[30] A. Karimi, B. Nasernejad, A. Morad Rashidi, A. Tavasoli, M. Pourkhalil, Fuel 117 (2014) 1045.
[31] P. Chen, F. Yang, A. Kostka, W. Xia, ACS Catal. 4 (2014) 1478.
[32] Z. Wei, J. Wang, S. Mao, D. Su, H. Jin, Y. Wang, F. Xu, H. Li, Y. Wang, ACS Catal. 5 (2015) 4783.
[33] W. Shi, B. Zhang, Y. Lin, Q. Wang, Q. Zhang, D.S. Su, ACS Catal. 6 (2016) 7844.
[34] A.R. Hajipoura, F. Rafiee, J. Iran Chem. Soc. 6 (4) (2009) 647.
[35] J.W. Lee, J.Y. Shin, Y.S. Chun, H.B. Jang, C.E. Song, A.S. Lee, Acc. Chem. Res. 43 (2010) 985.
[36] Y. Ren, T. Meng, J. Jia, H. Wu, Comput. Theor. Chem. 978 (2011) 47.
[37] Y.P. Patil, P.J. Tambade, K.M. Deshmukh, B.M. Bhanage, Catal. Today 148 (2009) 355.
[38] Q. Ma, W. Ding, M. Wu, T. Zhao, Y. Yoneyama, N. Tsubaki, Fuel 108 (11) (2013) 430.
[39] Y. Sun, C. Li, A. Zhang, Appl. Catal. A 522 (2016) 180.
[40] C.V. Rao, C.R. Cabrera, Y. Ishikawa, J. Phys. Chem. Lett. 1 (18) (2010) 2622.
[41] Z. Mo, S. Liao, Y. Zheng, Z. Fu, Carbon 50 (7) (2012) 2620.
[42] H. Deng, Q. Li, J. Liu, F. Wang, Carbon 112 (2017) 219.
[43] C. Domínguez, F.J. Pérez-Alonso, S.A. Al-Thabaiti, S.N. Basahel, A.Y. Obaid, A.O. Alyoubi, J.G. Fuente, S. Rojas, Electrochim. Acta 157 (2015) 158.
[44] A.O. Al-Youbi, J.L.G.D.L. Fuente, F.J. Pérez-Alonso, A.Y. Obaid, J.L.G. Fierro, M.A. Peña, M.A. Salama, S. Rojas, Appl. Catal. B-Environ. 150–151 (11) (2014) 21.
[45] X.L. Ling, Y.Z. Wei, L.M. Zou, S. Xu, Colloid. Surf. A 421 (11) (2013) 9.
[46] J. Bian, M. Xiao, S. Wang, Y.X. Lu, Y.Z. Meng, Appl. Surf. Sci. 255 (16) (2009) 7188.
[47] S.Z. Kang, D. Yin, X. Li, J. Mu, Colloid. Surf. A 384 (1) (2011) 363.
[48] S. Murugesan, K. Myers, V. Subramanian, Appl. Catal. B-Environ. 103 (3) (2011) 266.
[49] F. Avilés, J.V. Cauich-Rodríguez, L. Moo-Tah, A. May-Pat, R. Vargas-Coronado, Carbon 47 (13) (2009) 2970.
[50] S. Xue, Z. Xu, Y. Tang, C. Ji, ACS Appl. Mater. Interfaces 8 (2016) 19135.
[51] W. Xiong, K. Wang, X. Liu, F. Hao, H. Xiao, P. Liu, H. Luo, Appl. Catal. A 514 (2016) 126.
[52] N. Liu, L. Yin, C. Wang, L. Zhang, N. Lun, D. Xiang, Y. Qi, R. Gao, Carbon 48 (2010) 3579.
[53] Y. Sun, K. Li, J. Zhao, J. Wang, N. Tang, D. Zhang, T. Guan, Z. Jin, J. Colloid Interf. Sci. 526 (2018) 174.
[54] S. Liang, G. Li, R. Tian, J. Mater. Sci. 51 (2016) 3513.
[55] X. Ling, Y. Wei, L. Zou, S. Xu, Appl. Surf. Sci. 276 (2013) 159.
[56] A. Chakravarty, K. Bhowmik, A. Mukherjee, G. De, Langmuir 31 (2015) 5210.
[57] O. Podyacheva, A. Lisitsyn, L. Kibis, A. Stadnichenko, A. Boronin, E. Slavinskaya, O. Stonkus, S. Yashnik, Z. Ismagilov, Catal. Today 301 (2018) 125.
[58] W. Liu, Y. Chen, H. Qi, L. Zhang, W. Yan, X. Liu, X. Yang, S. Miao, W. Wang, C. Liu, A. Wang, J. Li, T. Zhang, Angew Chem. Int. Ed. 57 (2018) 7071.
[59] W. Ma, N. Wang, T. Tong, L. Zhang, K. Andrew Lin, X. Han, Y. Du, Carbon 137 (2018) 291.
[60] Y. Zhao, K. Watanabe, K. Hashimoto, J. Mater. Chem. A 1 (2013) 1450.
[61] H. Fang, J. Zheng, X. Luo, J. Du, A. Roldan, S. Leoni, Y. Yuan, Appl. Catal. A 529 (2017) 20.
[62] B. Solsona, P. Concepción, S. Hernández, B. Demicol, J.M.L. Nieto, Catal. Today 180 (1) (2012) 51.
[63] Z. Li, J. Liu, C. Xia, F. Li, ACS Catal. 3 (2013) 2440.
[64] H.J. Freund, Angew Chem. Int. Ed. 36 (1997) 452.
[65] X. Ning, Y. Li, B. Dong, H. Wang, H. Yu, F. Peng, Y. Yang, J. Catal. 348 (2017) 100.
[66] M. Gousi, C. Andriopoulou, K. Bourikas, S. Ladas, M. Sotiriou, C. Kordulis, A. Lycourghiotis, Appl. Catal. A 536 (2017) 45.
[67] C. Li, A. Zhao, W. Xia, C. Liang, M. Muhler, J. Phys. Chem. C 116 (2012) 20930.
[68] J. Long, K. Shen, Y. Li, ACS Catal. 7 (2017) 275.
[69] J. Li, J. Liu, H. Zhou, Y. Fu, ChemSusChem 9 (2016) 1339.